J. Fluid Mech. (2021), *vol*. 910, A49, doi:10.1017/jfm.2020.1006

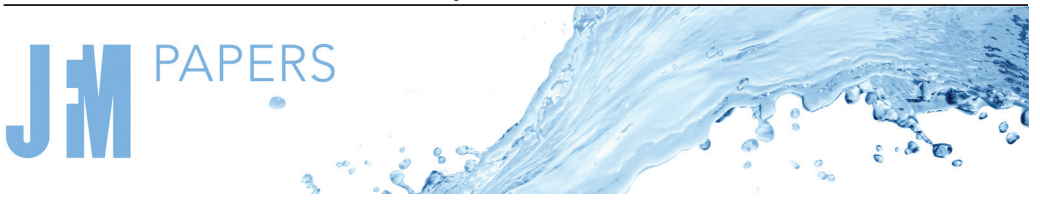

Upstream-propagating waves induced by steady current over a rippled bottom: theory and experimental observation

Jun Fan[1,2], Jinhai Zheng[1,2,†], Aifeng Tao[1,2] and Yuming Liu[3,†]

[1]Key Laboratory of Ministry of Education for Coastal Disaster and Protection, Hohai University, Nanjing 210024, PR China

[2]College of Harbour, Coastal and Offshore Engineering, Hohai University, Nanjing 210024, PR China

[3]Department of Mechanical Engineering, Massachusetts Institute of Technology, Cambridge, MA 02139, USA

(Received 17 August 2020; revised 26 October 2020; accepted 5 November 2020)

We theoretically and experimentally investigate the mechanism underlying the generation of upstream-propagating waves induced by a steady current over a horizontal bottom with a patch of sinusoidal ripples. By considering the triad resonant wave–ripple interactions involving two unsteady wave components (which have the same frequency but different wavenumbers) and one bottom ripple component in the presence of a steady uniform current, we derive the general condition under which unsteady upstream- and/or downstream-propagating waves can be induced. The frequency and wavenumbers of the induced propagating waves are given by the triad resonance condition in terms of current speed, water depth and bottom ripple wavenumber. By means of a multiple-scale perturbation analysis, we obtain the nonlinear amplitude evolution equations governing the spatio-temporal evolution of resonance-generated waves. Based on these equations, we find that the amplitude of the generated upstream-propagating waves is dramatically amplified when the associated triad resonance occurs in the neighbourhood of the critical current speed/frequency (corresponding to zero group velocity of unsteady waves in the presence of a current). A series of laboratory experiments in a long wave flume with wide ranges of current speeds and water depths are conducted to verify the theory. The experiments confirm the observation of the phenomenon of upstream-propagating wave generation in a steady flow over a rippled bottom. In particular, the experimental measurements of the kinematics of upstream-propagating waves as well as the critical flow condition for the observation of such wave generation compare well with the theoretical prediction.

Key words: surface gravity waves, wave scattering, nonlinear instability

† Email addresses for correspondence: jhzheng@hhu.edu.cn, yuming@mit.edu

1. Introduction

Understanding the characteristic behaviours of open channel flow over a rippled bottom is a classical hydrodynamic problem. There has been a great deal of investigation of this fundamental problem owing to the close relevance to the modelling and prediction of flow dynamics and bottom morphological evolution in estuarine and near-shore regions. An early study treated the relatively simple case of steady uniform flow over an infinitely extended horizontal sinusoidal wavy bottom (Lamb 1932). Under the assumption of potential flow, the first-order (in the wave steepness) solution of the steady free-surface profile (also known as stationary waves) is well known. The solution contains a singularity at which the steady wave amplitude becomes unbounded. The singularity corresponds to the resonance flow speed that is equal to the phase speed of the propagating wave with the same wavelength as the bottom ripple. The solution has been validated by flume experiments for supercritical flows (Kennedy 1963). The inclusion of up to the third-order wave–ripple interactions removes the singularity and yields a regularized bounded nonlinear solution of steady wave profile in the neighbourhood of the resonance flow speed (Mei 1969).

In addition to the stationary waves, Binnie (1960) observed, in flume experiments, the presence of unsteady waves when a steady current passes through a channel with periodic uneven sidewalls. To understand this phenomenon, interest then shifted to the fundamental instability problem of stationary gravity waves associated with steady flow over a wavy bottom (or sidewalls). Based on a linear stability analysis, Yih (1976) found that the stationary wave is unstable to a pair of small downstream-propagating wave disturbances of the same frequency for any bottom wavenumber k_b if the Froude number of the flow $F_r \equiv U/(gh)^{1/2} > 1$, where U represents the constant current speed, h the mean water depth and g the gravitational acceleration. If $F_r \leqslant 1$, the instability is obtained only for $k_b \geqslant k_{bc}$, where the cutoff wavenumber k_{bc} is a function of F_r^2. The inherent mechanics of the instability is believed to be associated with the triad resonant interactions (Phillips 1966; Hasselmann 1967) among the two downstream-propagating wave disturbances and the stationary surface wave or bottom ripples. Based on the nonlinear amplitude evolution equations of the interacting waves in the resonant triad, Raj & Guha (2019) showed that the amplitudes of both downstream-propagating disturbances can grow exponentially with time by taking energy from the base stationary wave, confirming the result of Yih (1976). Additionally, McHugh (1988) extended the stability analysis of Yih (1976) to the problem of steady channel flow over periodic wavy walls and found, based on the argument of triad resonances, the existence of multiple pairs of unsteady wave disturbances to which the steady flow is unstable. The surface tension effect on the instability of steady flow over a wavy bottom has also been investigated (McHugh 1992).

In a relatively small-scale flume experiment of steady flow over a bottom patch of sinusoidal ripples, Kyotoh & Fukushima (1997) observed an interesting phenomenon that a regular surface wave train of significant amplitude advancing against the incoming current is produced when the steady flow reaches the critical speed, which varies with water depth and bottom ripple wavenumber. The experimental data of the flow condition on the observation of such upstream-advancing waves does not match that from the linear instability result of Yih (1976). Kyotoh & Fukushima (1997) then postulated that the observed upstream-advancing waves result from the nonlinear instability of the steady base flow and aimed to corroborate the experimental data with the Benjamin–Feir instability. Kyotoh & Fukushima (1997) analysed the modulational instability of the nonlinear steady flow near the resonance flow speed (Mei 1969). The predicted flow condition for the

nonlinear instability as well as the period of upstream-propagating waves do not agree with the experimental data. The exact mechanism controlling the upstream-propagating wave generation in the steady flow over a rippled bottom remains unclear and thus needs to be investigated.

In this work, we carry out a theoretical and experimental investigation of the generation mechanism of upstream-propagating waves in a steady uniform flow over a horizontal rippled bottom. From the perspective of nonlinear resonant wave–wave interactions, we examine the kinematic features of propagating waves that could be generated through triad resonant wave–ripple interactions in the presence of a uniform current. By means of a multiple-scale perturbation analysis, we study the temporal and spatial evolution process of the wave generation and investigate the influence of flow and bottom ripple parameters on the development of upstream-propagating waves. From the theoretical analysis, we deduce that a significant upstream-propagating wave can be induced by triad resonant wave–ripple interactions under the flow condition for which the group velocity of the associated upstream-propagating waves is near zero over the rippled bottom. To assist in understanding the wave generation mechanism and verify the theory, we conduct relatively large-scale flume experiments with wide ranges of flow and bottom parameter values. The generation of upstream-propagating waves in a steady flow over a horizontal bottom with a patch of bottom ripples is observed. The experimental measurements of the frequency and wavenumber of the upstream-propagating waves as well as the corresponding flow conditions corroborate well with the theoretical prediction.

The remainder of the paper is organized as follows. The general boundary-value problem (BVP) governing the unsteady wave motion in the presence of a uniform constant current is formulated in § 2. The triad resonant condition for the interaction of two surface wave components and one bottom ripple component is examined in § 3. The theoretical results of wave generation from the multiple-scale perturbation analysis are described in § 4. The laboratory flume experiments and major experimental data are presented in § 5. The comparisons of the experiments with the theory are made and discussed in detail in § 6. Finally, § 7 contains the conclusions.

2. Problem statement

We consider the general two-dimensional problem of nonlinear wave propagation over a horizontal bottom with a patch of sinusoidal ripples in the presence of a uniform current. Figure 1 shows a schematic diagram of the problem. We define a right-handed Cartesian coordinate system O–xz, in which the origin O is located on the mean water line, the x-axis points in the horizontal direction and the z-axis is positive upwards. The positions of the free surface and bottom are denoted by $z = \eta(x, t)$ and $z = -h + \zeta(x)$, respectively, where t is time, $\eta(x, t)$ represents the instantaneous wave elevation, $\zeta(x)$ describes the rippled bottom variation and h is the mean water depth. The current is assumed to move along the x-direction with a speed of U.

In the context of potential flow assumptions, the fluid motion is described by the velocity potential $\Phi(x, z, t)$, which can be decomposed into two parts,

$$\Phi(x, z, t) = Ux + \phi(x, z, t), \tag{2.1}$$

where the term Ux represents the velocity potential of the uniform current and $\phi(x, z, t)$ denotes the perturbation velocity potential associated with the wave motion in the flow. The BVP governing the wave motion consists of the Laplace equation

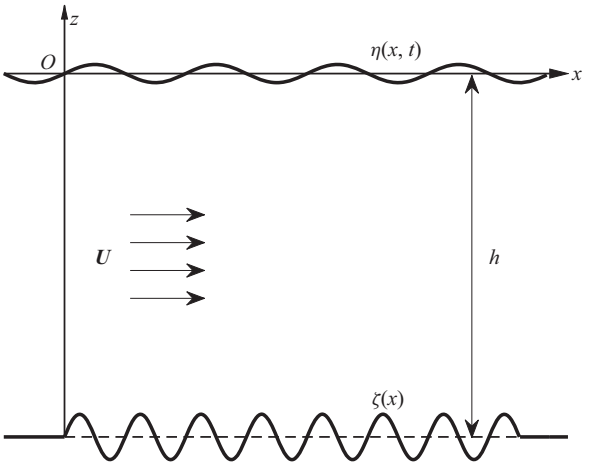

Figure 1. Schematic diagram of wave propagation over a patch of corrugated bottom in the presence of a uniform current.

$$\nabla^2\phi = 0, \quad -h + \zeta(x) \leqslant z \leqslant \eta(x,t), \tag{2.2}$$

where $\nabla \equiv (\partial/\partial x, \partial/\partial z)$, the nonlinear kinematic and dynamical free-surface boundary conditions,

$$\eta_t + (U + \phi_x)\eta_x = \phi_z, \quad z = \eta(x,t), \tag{2.3}$$

$$\phi_t + U\phi_x + \tfrac{1}{2}(\phi_x^2 + \phi_z^2) + gz = 0, \quad z = \eta(x,t), \tag{2.4}$$

and the impervious condition on the rippled bottom,

$$\phi_z = (U + \phi_x)\zeta_x, \quad z = -h + \zeta(x). \tag{2.5}$$

In the present study, we assume that the bottom ripples contain a monochromatic wave component with $\zeta(x) = (b/2)\,\mathrm{e}^{\mathrm{i}k_b x} + \text{c.c.}$, where b and k_b are the amplitude and wavenumber of the bottom ripples, respectively, and c.c. denotes the complex conjugate of the preceding term. The steepness of the bottom ripples is assumed to be small, i.e. $k_b b \ll 1$.

The wave motion can be further split into steady and unsteady components: $\phi(x,z,t) \equiv \phi_s(x,z) + \phi_u(x,z,t)$ and $\eta(x,t) \equiv \eta_s(x) + \eta_u(x,t)$, where ϕ_s/ϕ_u and η_s/η_u represent the velocity potential and free-surface elevation of the steady/unsteady wave motion. The BVP for the steady wave motion directly follows from the neglect of the time-dependent terms in (2.2), (2.3), (2.4) and (2.5). It is well known that for an infinitely extended rippled bottom, the solution of the linearized steady problem is singular at the resonance current speed equal to the phase speed of the surface waves with a wavenumber of k_b (Richardson 1920; Lamb 1932). By accounting for up to the third-order nonlinear wave–ripple interactions, Mei (1969) regularized the singularity and derived a uniformly valid solution in the neighbourhood of the resonance current speed by the use of high-order perturbation analysis.

Substitution of the steady and unsteady decompositions of ϕ and η into (2.2), (2.3), (2.4) and (2.5) (with the steady wave quantities subtracted) yields the nonlinear BVP for ϕ_u and η_u, governing the unsteady wave motion. The associated linear homogeneous problem

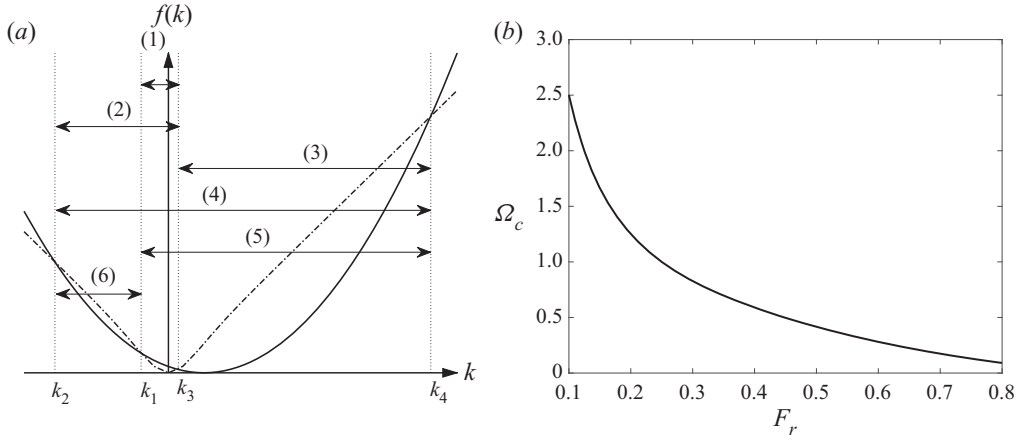

Figure 2. (*a*) Schematic illustration of four wavenumber solutions of the dispersion relation (2.8) for given ω, U and h: $f(k) = (\omega - kU)^2$ (——) and $g|k|\tanh|k|h$ (— · —). The six pairs of free unsteady wave components that can possibly form resonance triads with the bottom ripples are marked. (*b*) Dimensionless critical frequency $\Omega_c = \omega_c(h/g)^{1/2}$ as a function of the Froude number $F_r = U/(gh)^{1/2}$.

provides the solution of freely propagating waves in water of constant depth in the presence of a uniform current:

$$\phi_u^{(1)} = -\frac{\mathrm{i}gA}{2(\omega - kU)}\frac{\cosh(|k|(z+h))}{\cosh(|k|h)}\exp(\mathrm{i}(kx - \omega t)) + \text{c.c.} \tag{2.6}$$

and

$$\eta_u^{(1)} = \frac{A}{2}\exp(\mathrm{i}(kx - \omega t)) + \text{c.c.}, \tag{2.7}$$

where A is the complex wave amplitude. The frequency ω and wavenumber k are related by the dispersion relation

$$(\omega - kU)^2 = g|k|\tanh(|k|h). \tag{2.8}$$

It is known that, for a given U, four real wavenumber solutions of the dispersion relation (2.8) exist if ω is smaller than the critical frequency ω_c. The four solutions are given by the intersections of two definite curves corresponding to the left- and right-hand sides of (2.8), as illustrated in figure 2(*a*). For clarity in description, the four wavenumbers are respectively denoted as k_1, k_2, k_3 and k_4 with $k_2 < k_1 < k_3 < k_4$ (Mei, Stiassnie & Yue 2005). In general, $k_1, k_2 < 0$ while $k_3, k_4 > 0$. At $\omega = \omega_c$, wavenumbers k_1 and k_2 are equal. For $\omega > \omega_c$, wavenumbers k_1 and k_2 become pure complex numbers and only two real solutions (k_3 and k_4) of (2.8) exist. The normalized critical frequency, $\Omega_c \equiv \omega_c(h/g)^{1/2}$, is a function of the Froude number $F_r \equiv U/(gh)^{1/2}$, which is displayed in figure 2(*b*) for a wide range of F_r. In the deep-water limit (Mei *et al.* 2005), $\omega_c(h/g)^{1/2} \to (4F_r)^{-1}$ as $F_r \to 0$. We note that, as in deep water, both the crest and the energy of the k_1 wave propagate upstream, since it has negative phase and group speeds; the crest of the k_2 wave moves upstream, while the wave energy moves downstream, since this wave has a negative phase speed but a positive group speed; and the crest and energy of the k_3 and k_4 waves propagate downstream, as their phase and group speeds are positive.

The interest of the present study is on the influences of nonlinear interactions of current, surface waves and bottom ripples on the development of upstream-propagating waves

when a steady current passes over a rippled bottom. We shall address this problem from the perspective of resonant unsteady wave interactions with bottom ripples and steady waves.

3. Triad resonance condition

In the presence of a steady current, similarly to the classical Bragg scattering of surface wave by bottom ripples (Mei 1985; Mei *et al.* 2005), the second-order triad resonance involving two unsteady surface wave components and one bottom ripple (or steady surface wave) component can occur under the condition

$$k_m - k_n = k_b \quad \text{and} \quad \omega_m - \omega_n = 0, \tag{3.1a,b}$$

where $k_{m/n}$ and $\omega_{m/n}$ are the wavenumbers and frequencies of the mth and nth unsteady wave components. The wavenumber $k_{m/n}$ and the corresponding frequency $\omega_{m/n}$ must satisfy the dispersion relation (2.8). Without loss of generality, we assume $\omega_{m/n} > 0$, while $k_{m/n}$ could be positive or negative. The condition (3.1*a*,*b*) directly follows from the general triad resonance condition for three surface wave components (Phillips 1966) by treating the bottom ripple as a steady wave component with positive wavenumber ($k_b > 0$) and zero frequency.

To satisfy the condition (3.1*a*,*b*), the surface wave components must be two of the four free wave components (of wavenumbers k_1, k_2, k_3 and k_4) that correspond to the same frequency ω. There are possibly six wavenumber combinations that can form the resonance triads (McHugh 1988, 1992; Raj & Guha 2019) with the corresponding condition given by

$$\left.\begin{array}{llll} (1) & k_3 - k_1 = k_b \quad \text{and} \quad \omega_{3/1} = \omega, & (4) & k_4 - k_2 = k_b \quad \text{and} \quad \omega_{4/2} = \omega, \\ (2) & k_3 - k_2 = k_b \quad \text{and} \quad \omega_{3/2} = \omega, & (5) & k_4 - k_1 = k_b \quad \text{and} \quad \omega_{4/1} = \omega, \\ (3) & k_4 - k_3 = k_b \quad \text{and} \quad \omega_{4/3} = \omega, & (6) & k_1 - k_2 = k_b \quad \text{and} \quad \omega_{1/2} = \omega. \end{array}\right\} \tag{3.2}$$

The wavenumber combinations in these six cases are sketched in figure 2(*a*). For given U, k_b and h, the frequency and wavenumbers of the two unsteady wave components in the resonance triad can be obtained from the following relations:

$$\left.\begin{array}{c} k_n U + \alpha_n \sqrt{g k_n \tanh(k_n h)} = k_m U + \alpha_m \sqrt{g k_m \tanh(k_m h)}\,, \\ k_m = k_n + k_b, \\ \omega = k_n U + \alpha_n \sqrt{g k_n \tanh(k_n h)}\,, \end{array}\right\} \tag{3.3}$$

with $(m, n) = (3, 1)$ for (1), $(m, n) = (3, 2)$ for (2), $(m, n) = (4, 3)$ for (3), $(m, n) = (4, 2)$ for (4), $(m, n) = (4, 1)$ for (5) and $(m, n) = (1, 2)$ for (6), and with $\alpha_{1/2/3} = 1$ and $\alpha_4 = -1$. Specifically, we first solve for k_n from the first equation of (3.3), and then obtain k_m and ω from the second and third equations of (3.3), respectively.

For given F_r and $k_b h$, it can be shown that there are at most two of the six triads that can exist (McHugh 1988, 1992). Figure 3 displays the specific region in the domain of F_r and $k_b h$ inside which each of the six triads exists. The boundary curves separating neighbouring regions can be specifically defined. By rewriting the first equation of (3.3) in the form

$$k_b U = \alpha_n \sqrt{g k_n \tanh(k_n h)} - \alpha_m \sqrt{g k_m \tanh(k_m h)}\,, \tag{3.4}$$

we can easily figure out the boundary beyond which the meaningful solution of k_n for the triad (m) does not exist. The boundary curve between triads (2) and (3) is found to be

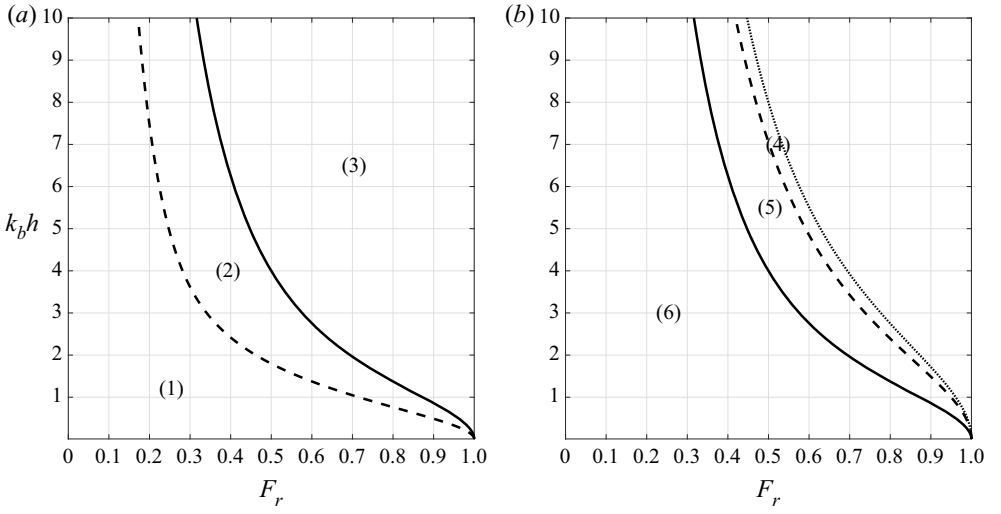

Figure 3. The specific regions in the domain of F_r and k_bh for each of the six triads: (*a*) for triads (1), (2) and (3); and (*b*) for (4), (5) and (6). The solid and dashed lines separate the neighbouring regions, and the dotted line defines the outer boundary of the region for triad (4).

given by the same boundary curve as between triads (5) and (6), $F_r = [\tanh(k_bh)/k_bh]^{1/2}$. The outer boundary of triad (4), beyond which no triad (4) exists, is given by $F_r = [\tanh(k_bh/2)/(k_bh/2)]^{1/2}$. The boundaries separating the regions of triads (1) and (2) as well as that of (4) and (5) are determined by imposing an extra condition $k_1 = k_2$ in addition to (3.4). One sees from figure 2(*a*) that $k_1 = k_2$ is obtained when the curve for the left-hand side quantity of (2.8) is tangential to the curve for the right-hand side quantity of (2.8), corresponding to the following condition:

$$\tanh(k_nh) + k_nh(1 - \tanh^2(k_nh)) = -2F_r\sqrt{k_nh\tanh(k_nh)}\,. \tag{3.5}$$

From (3.4) and (3.5), we find the boundary of triads (1) and (2) and that of (4) and (5), as shown in figure 3.

For illustration, figures 4 and 5 display the dimensionless wavenumber k_mh and the corresponding dimensionless frequency Ω for one of the two unsteady wave components in the resonant triad (with $k_m - k_n = k_b$) as a function of the Froude number F_r with three sample dimensionless bottom wavenumbers ($k_bh = 3.0$, 6.0 and 9.0) for all six triads. For fixed k_bh, the triad transits from (1) to (2) and then to (3) as well as from (6) to (5) and then to (4) as F_r increases from zero to infinity. The wavenumber of the other wave component in the triad can be obtained from the relation $k_n = k_m - k_b$.

4. Multiple-scale perturbation analysis

4.1. *Amplitude evolution equations of resonant interacting waves*

In order to understand the wave generation mechanism due to the triad resonance, we derive the amplitude evolution equations of the interacting wave components by means of the classical multiple-scale perturbation analysis. Since the procedure of the multiple-scale analysis for wave resonance is standard (Mei 1985; Kirby 1988; Mei *et al.* 2005), we only outline the key procedures and intermediate results of the analysis in appendix A. For illustration, we consider a general resonant triad in the presence of a steady uniform

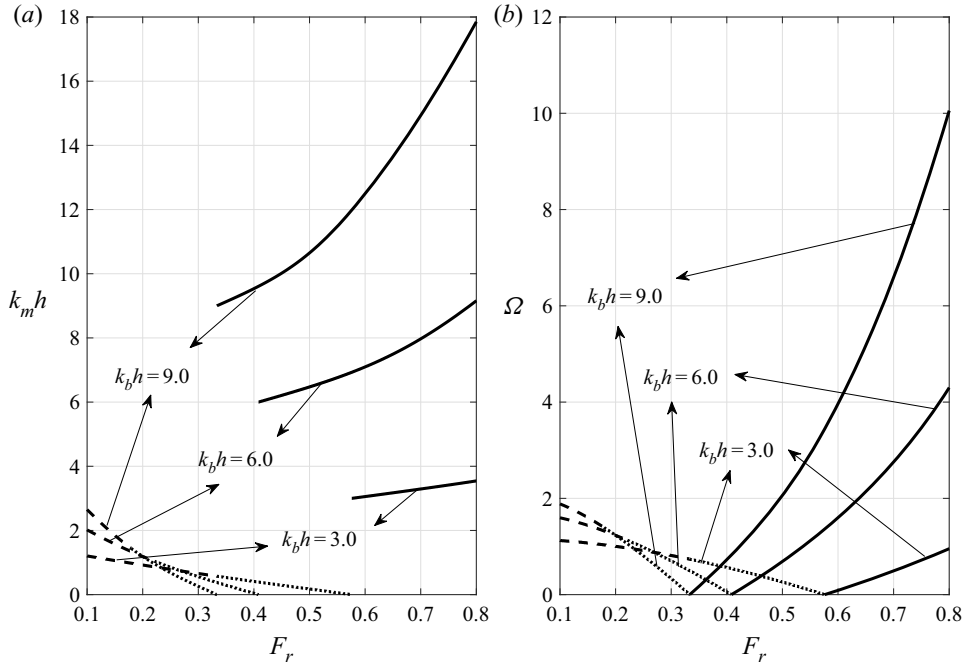

Figure 4. Dimensionless (a) wavenumber $k_m h$ and (b) frequency $\Omega = \omega(h/g)^{1/2}$ for one of the two unsteady wave components in the resonant triad (with $k_m - k_n = k_b$) as a function of F_r with three dimensionless bottom wavenumbers $k_b h = 3.0$, 6.0 and 9.0 for triad (1) (- - -), (2) (· · · · · ·) and (3) (——).

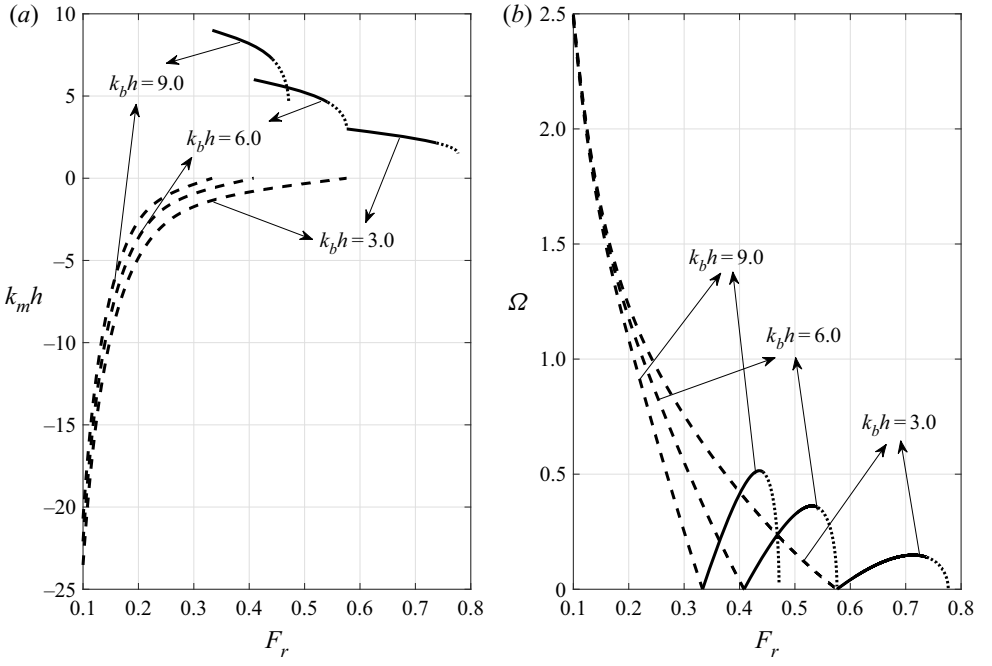

Figure 5. Dimensionless (a) wavenumber $k_m h$ and (b) frequency $\Omega = \omega(h/g)^{1/2}$ for one of the two unsteady wave components in the resonant triad (with $k_m - k_n = k_b$) as a function of F_r with three dimensionless bottom wavenumbers $k_b h = 3.0$, 6.0 and 9.0 for triad (6) (- - -), (5) (——) and (4) (· · · · · ·).

current, which is formed by two propagating surface wave components (with wavenumbers k_m and k_n) and one stationary bottom ripple component (with wavenumber k_b), under the exact resonance condition ($k_m - k_n = k_b$ and $\omega_m = \omega_n = \omega$). The total wave solution of the velocity potential for the resonant triad can be expressed in the form

$$\begin{aligned}\phi^{(1)}(x,z,t) = &-\frac{gA_m}{\omega - k_m U}\frac{\cosh(k_m(z+h))}{\cosh(k_m h)}\left[\frac{\mathrm{i}}{2}\exp(\mathrm{i}(k_m x - \omega t))\right]\\ &-\frac{gA_n}{\omega - k_n U}\frac{\cosh(k_n(z+h))}{\cosh(k_n h)}\left[\frac{\mathrm{i}}{2}\exp(\mathrm{i}(k_n x - \omega t))\right]\\ &-Ub\frac{g\cosh(k_b z) + U^2 k_b \sinh(k_b z)}{g\sinh(k_b h) - U^2 k_b \cosh(k_b h)}\left[\frac{\mathrm{i}}{2}\exp(\mathrm{i}k_b x)\right] + \text{c.c.},\end{aligned} \tag{4.1}$$

where A_m and A_n are the complex amplitudes of the propagating waves. The third term on the right-hand side of (4.1) represents the velocity potential associated with the stationary wave resulting from the uniform current passing over bottom ripples. At the resonance, A_m and A_n have slow x and slow t dependences.

Through a multiple-scale perturbation analysis summarized in appendix A, we obtain the following coupled equations governing the evolution of A_m and A_n:

$$\left.\begin{aligned}\frac{\partial A_m(x,t)}{\partial t} + C_m\frac{\partial A_m(x,t)}{\partial x} &= \mathrm{i}A_n(x,t)\mathbb{P},\\ \frac{\partial A_n(x,t)}{\partial t} + C_n\frac{\partial A_n(x,t)}{\partial x} &= \mathrm{i}A_m(x,t)\mathbb{Q},\end{aligned}\right\} \tag{4.2}$$

where the group velocities of the propagating wave components, C_m and C_n, and the interaction coefficients $\mathbb{P}$ and $\mathbb{Q}$ are respectively given by (A26), (A27), (A28) and (A29). The two equations in (4.2) can be decoupled to yield the separate second-order partial differential equations for $A_m(x,t)$ and $A_n(x,t)$:

$$\left.\begin{aligned}\frac{\partial^2 A_m(x,t)}{\partial t^2} + (C_m + C_n)\frac{\partial^2 A_m(x,t)}{\partial x \partial t} + C_m C_n\frac{\partial^2 A_m(x,t)}{\partial x^2} + \mathbb{P}\mathbb{Q}A_m(x,t) &= 0,\\ \frac{\partial^2 A_n(x,t)}{\partial t^2} + (C_m + C_n)\frac{\partial^2 A_n(x,t)}{\partial x \partial t} + C_m C_n\frac{\partial^2 A_n(x,t)}{\partial x^2} + \mathbb{P}\mathbb{Q}A_n(x,t) &= 0.\end{aligned}\right\} \tag{4.3}$$

With proper boundary and initial conditions, we can solve the above equations to obtain the solutions of $A_m(x,t)$ and $A_n(x,t)$. It should be noted that the above equations are similar to those derived in Kirby (1988), who studied the current effects on Bragg resonant reflection of surface water waves by sand bars. The specific cases addressed in Kirby (1988) are associated with triads (1) and (5) with the k_3 or k_4 wave component as the incident wave and the k_1 component as the reflected wave. The present study focuses on the growth of unsteady waves (from small initial disturbances) in steady current interaction with bottom ripples without incident waves.

Triad no.	Wavenumber combination	Parameter $\mathbb{PQ}$	Temporal evolution behaviour
1	$k_3 - k_1 = k_b$	$\geqslant 0$	Stable
2	$k_3 - k_2 = k_b$	$\geqslant 0$	Stable
3	$k_4 - k_3 = k_b$	< 0	Unstable
4	$k_4 - k_2 = k_b$	< 0	Unstable
5	$k_4 - k_1 = k_b$	< 0	Unstable
6	$k_1 - k_2 = k_b$	$\geqslant 0$	Stable

Table 1. Temporal stability of steady flow over the infinitely extended horizontal rippled bottom derived based on the triad resonance.

4.2. *Temporal evolution*

If the rippled bottom extends indefinitely in the x-direction, we can consider $A_m(x, t)$ and $A_n(x, t)$ to be independent of x. In this special case, equations (4.3) reduce to

$$\left.\begin{aligned} \frac{\mathrm{d}^2 A_m(t)}{\mathrm{d}t^2} &= -\mathbb{PQ}A_m(t), \\ \frac{\mathrm{d}^2 A_n(t)}{\mathrm{d}t^2} &= -\mathbb{PQ}A_n(t). \end{aligned}\right\} \tag{4.4}$$

For given initial values of $A_m(0) = A_{m0}$ and $A_n(0) = A_{n0}$, we solve (4.4) for $A_m(t)$ and $A_n(t)$ to obtain

$$\left.\begin{aligned} A_m(t) &= \frac{1}{2}\left(A_{m0} + \frac{\mathrm{i}A_{n0}\mathbb{P}}{\gamma}\right)\mathrm{e}^{\gamma t} + \frac{1}{2}\left(A_{m0} - \frac{\mathrm{i}A_{n0}\mathbb{P}}{\gamma}\right)\mathrm{e}^{-\gamma t}, \\ A_n(t) &= \frac{1}{2}\left(A_{n0} + \frac{\mathrm{i}A_{m0}\mathbb{Q}}{\gamma}\right)\mathrm{e}^{\gamma t} + \frac{1}{2}\left(A_{n0} - \frac{\mathrm{i}A_{m0}\mathbb{Q}}{\gamma}\right)\mathrm{e}^{-\gamma t}, \end{aligned}\right\} \tag{4.5}$$

where the parameter γ is defined as

$$\gamma = \sqrt{-\mathbb{PQ}}\,. \tag{4.6}$$

If $\mathbb{PQ} \geqslant 0$, γ is imaginary (or zero) so that $|A_m(t)|$ and $|A_n(t)|$ are bounded in time. If $\mathbb{PQ} < 0$, γ is positive real so that $|A_m(t)|$ and $|A_n(t)|$ can grow exponentially with time. These indicate that the steady flow over the rippled bottom is stable (unstable) to a small disturbance consisting of wave components with wavenumbers k_m and k_n under the condition of $\mathbb{PQ} \geqslant 0$ ($\mathbb{PQ} < 0$). For all the six resonant triads, we numerically evaluate the value of $\mathbb{PQ}$ and present the temporal stability features in table 1. The result with triad (3) is consistent with the finding of Yih (1976) based on the linear instability analysis. The characteristic behaviour of the present result for flow over rippled bottoms is similar to that of McHugh (1986) for flow over wavy sidewalls.

4.3. *Spatial evolution*

When the bottom contains a finite-length patch of ripples, the interest is on the spatial amplitude variation of the interacting waves after long-time triad resonant interactions. This corresponds to solving for the steady-state solutions of $A_m(x, t) = A_m(x)$ and $A_n(x, t) = A_n(x)$. After removing the terms containing time derivatives in (4.3), we obtain

the spatial evolution equations for $A_m(x)$ and $A_n(x)$:

$$\left.\begin{aligned}\frac{\mathrm{d}^2A_m(x)}{\mathrm{d}x^2} &= -\frac{\mathbb{PQ}}{C_mC_n}A_m(x),\\ \frac{\mathrm{d}^2A_n(x)}{\mathrm{d}x^2} &= -\frac{\mathbb{PQ}}{C_mC_n}A_n(x).\end{aligned}\right\} \tag{4.7}$$

With two boundary conditions for each A_m and A_n, the above second-order differential equations can be solved to give the solutions of $A_m(x)$ and $A_n(x)$. Depending on the situation, the boundary conditions are specified in terms of the amplitude and/or the slope of the amplitude of the wave at the ends of the rippled bottom patch.

Since our interest in this work is on the generation mechanism of upstream-propagating waves by steady flow over a rippled bottom, we consider here the resonant triad with wavenumber combination (6). In this triad, the k_1 wave propagates upstream while the (energy of the) k_2 wave propagates downstream. The bottom ripples are assumed to be located within $0 \leqslant x \leqslant L$, outside of which the bottom is horizontal. For the boundary conditions, we consider that, at the downstream end of the rippled bottom patch ($x = L$), the k_2 wave has a small amplitude $A_2(x = L) = a_2$ and the k_1 wave has a negligibly small amplitude $A_1(x = L) = 0$ (as the generation of the k_1 wave by the triad resonance starts at $x = L$). From (4.2), these amplitude boundary conditions also imply the following conditions for the slope of the amplitude: $\mathrm{d}A_2/\mathrm{d}x(x = L) = 0$ and $\mathrm{d}A_1/\mathrm{d}x(x = L) = \mathrm{i}a_2\mathbb{P}/C_1$. With these boundary conditions, we solve (4.7) to obtain the solution of $A_1(x)$ and $A_2(x)$ given by

$$A_1(x) = \mathrm{i}\frac{a_2\mathbb{P}}{\theta C_1}\sinh(\theta(x-L)) \quad \text{and} \quad A_2(x) = a_2\cosh(\theta(x-L)), \tag{4.8a,b}$$

where the parameter θ is defined as

$$\theta = \sqrt{-\frac{\mathbb{PQ}}{C_1C_2}}\,. \tag{4.9}$$

If $\mathbb{PQ}/C_1C_2 \geqslant 0$, then θ is imaginary (or zero) and $A_{1,2}(x)$ are sine and/or cosine functions of x whose amplitudes are bounded. If $\mathbb{PQ}/C_1C_2 < 0$, then θ is positive real so that $A_{1,2}(x)$ can grow exponentially in x. Similar results for other triads can be obtained. Table 2 presents the spatial stability features of steady flow over the infinitely extended rippled bottom associated with all the six resonant triads.

As a numerical illustration, we consider one of the experimental cases to be described in the next section, for which we have $L/\lambda_b = 7.5$, $h/\lambda_b = 0.8$ and $\epsilon_b \equiv k_bb = 0.602$, where $\lambda_b = 2\pi/k_b$. For this bottom ripple configuration, figure 6 displays the values of $\mathbb{P}$, $\mathbb{Q}$, C_1 and C_2 as functions of F_r for the resonant triad (6). Both $\mathbb{P}$ and $\mathbb{Q}$ are positive, and, as expected, C_2 is positive while C_1 is negative. As a result, the parameter θ is real and positive, as shown in figure 7(*a*). The amplitudes of the generated unsteady waves $A_{1,2}(x)$ thus achieve an exponential growth with the interaction distance $L - x$. Figure 7(*b*) plots the maximum amplitude of the upstream-propagating k_1 wave obtained at $x = 0$ as a function of F_r, which is seen to decrease with increasing F_r.

We note that, since $\mathbb{PQ}$ is always positive, the parameter γ is pure imaginary from (4.6). In the case of bottom ripples that are uniformly extended to infinity, the unsteady wave components in the triad (6) do not grow exponentially with time. This indicates that the steady flow is temporally stable to the disturbance dominated by k_1 and k_2

Triad no.	Wavenumber combination	Parameter $\frac{\mathbb{PQ}}{C_m C_n}$	Spatial evolution behaviour
1	$k_3 - k_1 = k_b$	< 0	Unstable
2	$k_3 - k_2 = k_b$	$\geqslant 0$	Stable
3	$k_4 - k_3 = k_b$	< 0	Unstable
4	$k_4 - k_2 = k_b$	< 0	Unstable
5	$k_4 - k_1 = k_b$	$\geqslant 0$	Stable
6	$k_1 - k_2 = k_b$	< 0	Unstable

Table 2. Spatial stability of steady flow over the infinitely extended horizontal rippled bottom derived based on the triad resonance.

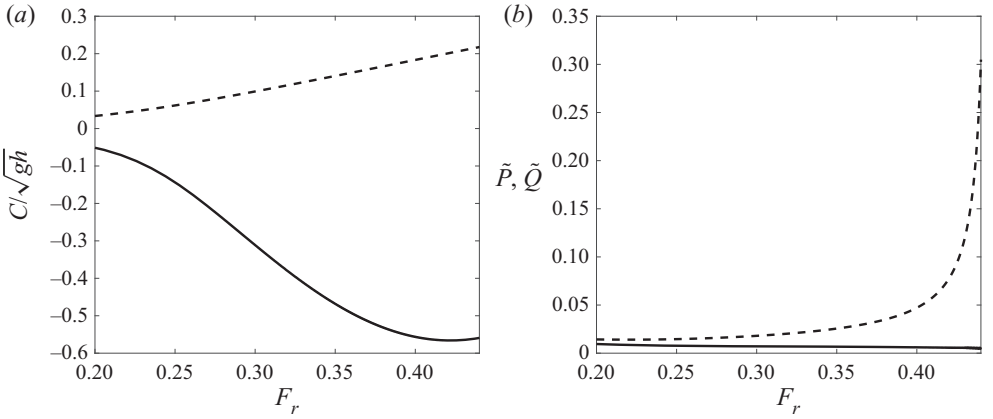

Figure 6. (*a*) Dimensionless group velocities $C_1/\sqrt{gh}$ (——) and $C_2/\sqrt{gh}$ (- - -), and (*b*) dimensionless interaction coefficients $\tilde{P} = \mathbb{P}\sqrt{h/g}$ (——) and $\tilde{Q} = \mathbb{Q}\sqrt{h/g}$ (- - -) as functions of F_r for resonant triad (6). (Here $L/\lambda_b = 7.5$, $h/\lambda_b = 0.8$ and $\epsilon_b = 0.602$.)

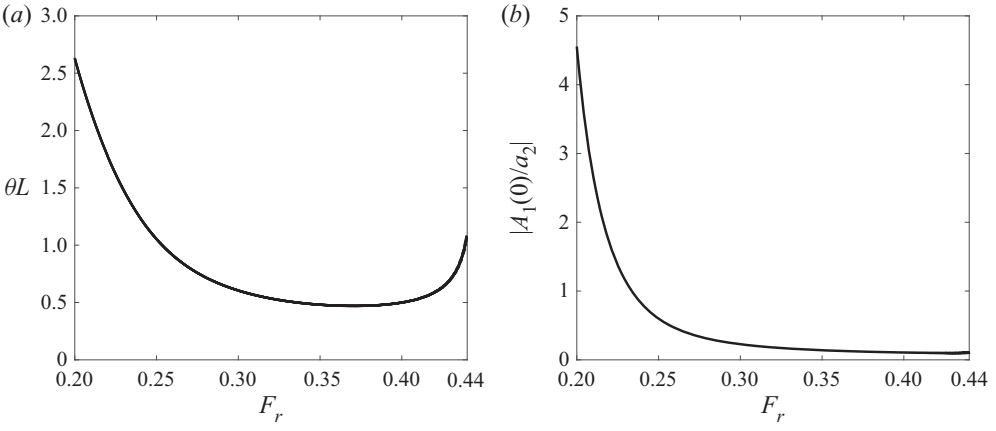

Figure 7. (*a*) Spatial growth rate θ and (*b*) maximum amplitude of the generated upstream-propagating wave, $|A_1(0)/a_2|$, as functions of F_r for resonant triad (6). (Here $L/\lambda_b = 7.5$, $h/\lambda_b = 0.8$, and $\epsilon_b = 0.602$.)

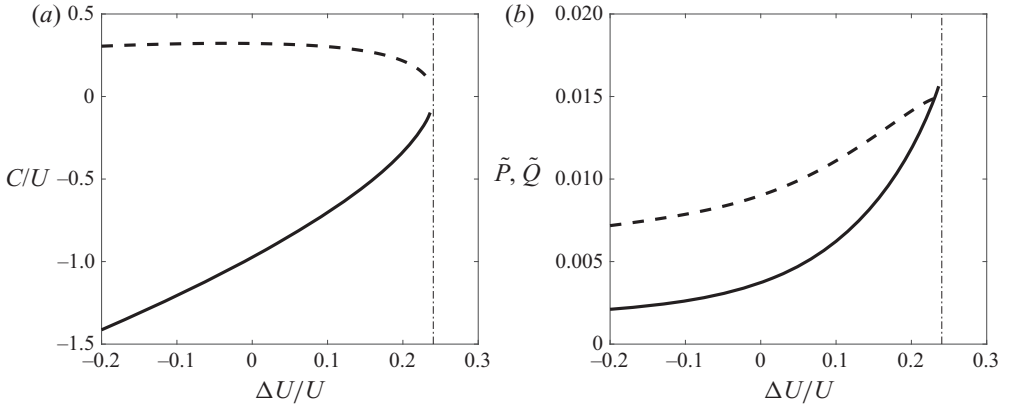

Figure 8. (*a*) Dimensionless group velocities C_1/U (——) and C_2/U (- - -), and (*b*) dimensionless interaction coefficients $\tilde{P} = \mathbb{P}\sqrt{h/g}$ (——) and $\tilde{Q} = \mathbb{Q}\sqrt{h/g}$ (- - -) as functions of current speed detuning $\Delta U/U$ from the exact resonance of triad (6). (Here $L/\lambda_b = 7.5$, $h/\lambda_b = 0.8$, $F_r = 0.30$ and $\epsilon_b = 0.602$.) The vertical line (— · —) represents the critical wave-flow condition.

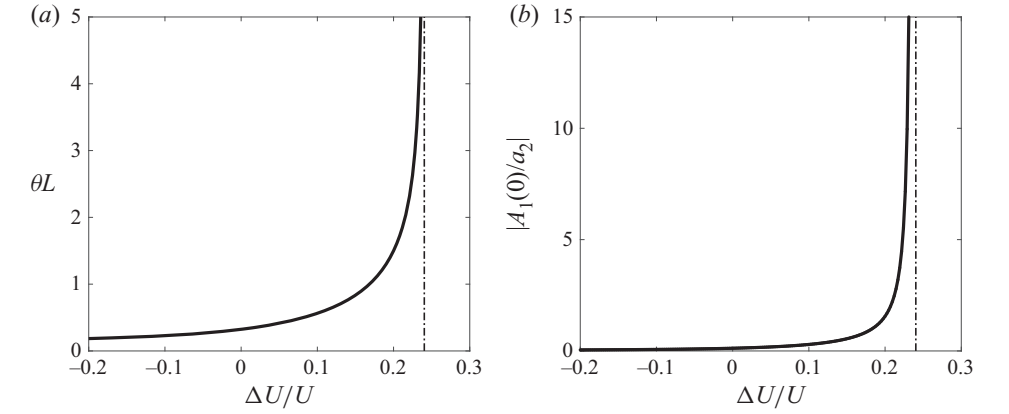

Figure 9. (*a*) Spatial growth rate θ and (*b*) maximum amplitude of generated upstream-propagating wave, $|A_1(0)/a_2|$, as functions of current speed detuning $\Delta U/U$ from the exact resonance of triad (6). (Here $L/\lambda_b = 7.5$, $h/\lambda_b = 0.8$, $F_r = 0.30$ and $\epsilon_b = 0.602$.) The vertical line (— · —) represents the critical wave-flow condition.

wave components. On the other hand, the above results show that the steady flow is spatially unstable to the k_1 and k_2 wave disturbance. This cannot be obtained by the temporal instability analysis (Yih 1976; Raj & Guha 2019).

If the resonance condition is not satisfied exactly, the detuning effect should be included in the solution. For illustration, we consider the detuning case in which the frequency (ω) of the generated unsteady waves is fixed while the current speed is shifted by a small amount ΔU from the speed U under the exact resonance condition (ω, U). The current speed detuning ΔU causes the wavenumber detunings Δk_1 and Δk_2 in k_1 and k_2, which can be calculated from the dispersion relation (with the use of ω and $U + \Delta U$). Since ω is invariant, the evolution equations for $A_1(x)$ and $A_2(x)$ are found to take the same form as (4.7) but with the coefficients evaluated at the detuning condition (i.e. ω, $U + \Delta U$, $k_1 + \Delta k_1$, $k_2 + \Delta k_2$). Taking the exact resonance at $F_r = 0.3$ (cf. figure 7*b*) as an example, we examine the solution of the resonance-generated upstream-propagating wave amplitude

as a function of the current speed detuning ΔU. Figure 8 shows C_1, C_2, $\mathbb{P}$ and $\mathbb{Q}$ while figure 9 shows the growth rate θ and maximum amplitude of the upstream-propagating wave $|A_1(0)|$ as functions of ΔU. It is seen that $|A_1(0)|$ becomes unbounded when the detuned current speed approaches the critical speed U_c (associated with the critical frequency $\omega_c = \omega$ considered). (The relation between U_c and the critical wave frequency ω_c is shown in figure 2*b*.) The singular behaviour of $|A_1(0)|$ results from the fact that θ becomes infinitely large as both C_1 and C_2 approach zero at U_c. These results indicate that, despite not at the exact resonance, the generation of upstream-propagating waves is substantially amplified in the neighbourhood of the critical current speed U_c (or critical frequency ω_c) due to the continuous buildup of energy in time for the unsteady k_1 and k_2 waves from the near-resonant triad interaction. We remark that the exact resonance does not occur at the critical flow condition under which $k_1 = k_2$, so that the triad resonance condition cannot be satisfied exactly.

5. Flume experiment

5.1. *Experimental apparatus and set-up*

To assist in understanding the phenomenon and verify the theoretical analysis of upstream-propagating wave generation in steady flow over a rippled bottom, we conducted a series of laboratory experiments in a relatively large-scale wave flume. The experimental set-up and configurations were optimized on the basis of Kyotoh's preliminary observation of upstream-advancing waves in a rather small wave flume (Kyotoh & Fukushima 1997). While the design and initial stage of the experiments as well as some preliminary qualitative observations were reported in Fan *et al.* (2016), the experimental set-up was improved and the experiments were recalibrated for better accuracy afterwards. The quantitative experimental results presented in this paper have not been reported elsewhere. For clarity and completeness, we summarize the latest primary experimental set-up, apparatus and calibrations below.

Figure 10 displays a sketch of the flume experiment set-up. Unlike in Kyotoh & Fukushima (1997), where the flume bottom was inclined to produce the incoming flow, we chose to use a horizontal flume bottom with a steady incoming flow generated by a water pump installed under the flume. The longitudinal distance between the upstream flow inlet and the downstream flow outlet is 51.0 m. The width and height of the flume are 1.0 m and 1.5 m, respectively. A patch of rippled wooden bottom consisting of seven-and-a-half sinusoidal ripples was installed in the relatively downstream side of the flume. The length of the rippled patch is $L_b = 1.80$ m, with the ripple wavelength equal to $\lambda_b = 0.24$ m. Four different ripple amplitudes of $b = 0.040$, 0.0305, 0.0265 and 0.023 m were used in the experiments. The corresponding ripple steepnesses are $\epsilon_b \equiv k_b b = 2\pi b/\lambda_b = 1.047$, 0.798, 0.694 and 0.602, respectively. The centre of the rippled patch is 33.0 m away from the upstream flow inlet. The rippled patch was embedded into the flume's flat bottom so that the average water depth is nearly equal to that over the flat bottom in the flume.

For each rippled bottom configuration, a wide range of water depths and incoming flow velocities, as displayed in table 3, were tested to ensure the observation of upstream-propagating waves. The range of parameters considered in table 3 is mainly for intermediate and shallow depths. In order to measure the free-surface oscillation, a total of 26 capacitive wave gauges were installed along the transverse centreline of the flume, 17 of which were uniformly set above the rippled bottom with a horizontal spatial interval of 0.12 m (equal to a half of the ripple wavelength), as shown in figure 10. For measuring the upstream-propagating waves, six wave gauges were set as three pairs upstream of the

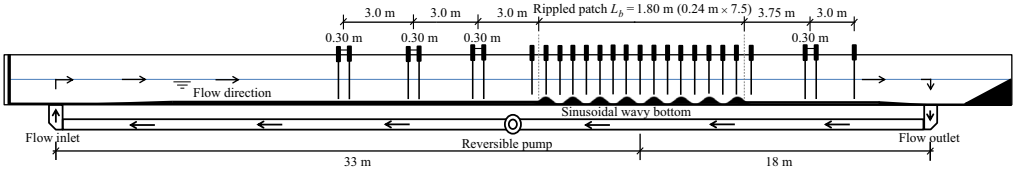

Figure 10. Sketch of the flume experiment set-up.

ϵ_b	$h/\lambda_b = 0.5$	$h/\lambda_b = 0.6$	$h/\lambda_b = 0.7$	$h/\lambda_b = 0.8$	$h/\lambda_b = 0.9$	$h/\lambda_b = 1.0$
0.602	0.20–0.35	0.24–0.35	0.26–0.33	0.28–0.33	—	—
0.694	0.20–0.32	0.20–0.33	0.23–0.33	0.24–0.33	0.24–0.33	—
0.798	—	0.15–0.33	0.15–0.33	0.15–0.33	0.15–0.33	0.20–0.33
1.047	—	0.20–0.30	0.18–0.28	0.18–0.28	0.18–0.28	0.18–0.28

Table 3. Ranges of Froude number F_r for different combinations of bottom ripple steepness and water depth that were tested with the observation of upstream-propagating waves in the experiments.

rippled bottom. Their distances from the upstream edge of the rippled patch are 3.0 m, 6.0 m and 9.0 m, respectively. In each pair, the distance between the wave gauges is set to be 0.30 m in order to calculate the wavelength of the upstream-propagating waves. (Note that this distance is much less than the wavelength of the observed upstream-propagating waves.) Besides these, another pair and one single wave gauges were placed downstream at 3.75 m and 6.75 m from the downstream edge of the rippled bottom, respectively. In the experiments, the flow conditions in the flume were calibrated before each test. The relationship between flow volume and voltage of the water pump's converter was acquired and utilized to calculate the input voltage for each experimental case.

5.2. *Experimental results*

We observed in the experiments that, for given rippled bottom configuration and water depth, unsteady waves that propagate against the steady incoming current are generated when the current reaches a narrow critical range of speed. For the current speed outside the critical range, such unsteady wave generation was not observed. For given ripple wavenumber, the critical range of current speed for upstream-propagating wave generation varies with water depth and ripple amplitude; and the frequency of the generated upstream-propagating waves is dependent on the current speed and water depth.

Figure 11 displays sample time variations and corresponding amplitude spectra of the free-surface elevations far upstream of the rippled bottom, above the rippled bottom and downstream of the rippled bottom in the case with $\epsilon_b = 0.798$, $h/\lambda_b = 0.6$ and $F_r = 0.280$. In the upstream location and over the rippled bottom, the free-surface elevation shows the presence of a dominant wave component at the same frequency $\omega = 2\pi f = 4.75$ rad s^{-1}. Downstream, the free-surface elevation is composed of small broad-banded wave components without a clear dominant component. Figure 12 shows a sample instantaneous free-surface pattern with the presence of monochromatic upstream-propagating waves.

Figure 13 plots the amplitude of the dominant component of the generated upstream-propagating waves, which is measured in the upstream flat horizontal bottom, as a function of current speed for different ripple steepnesses and water depths. The data

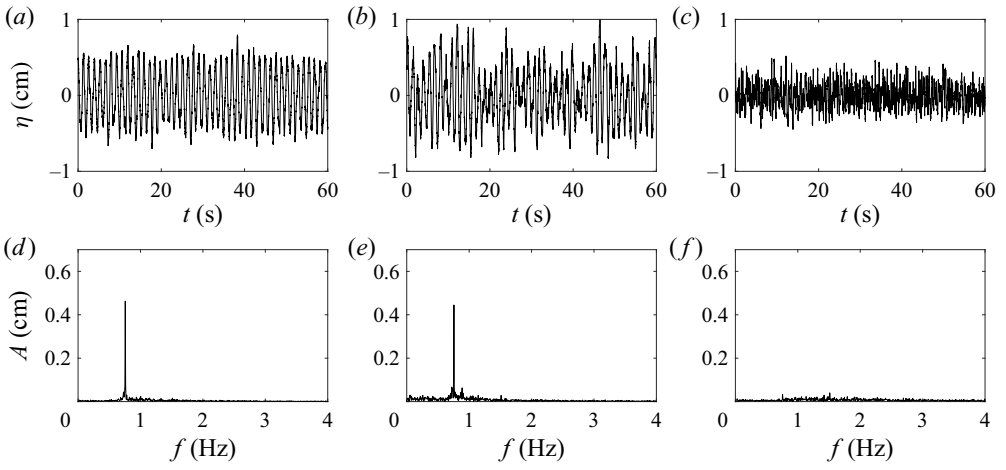

Figure 11. Time variations (*a–c*) and amplitude spectra (*d–f*) of the free-surface elevations (*a*,*d*) at the upstream side of the rippled bottom ($x/\lambda_b = -38.125$), (*b*,*e*) above the rippled bottom ($x/\lambda_b = 3.75$) and (*c*,*f*) at the downstream side of the rippled bottom ($x/\lambda_b = 22.5$). (Here $h/\lambda_b = 0.6$, $F_r = 0.280$ and $\epsilon_b = 0.798$.)

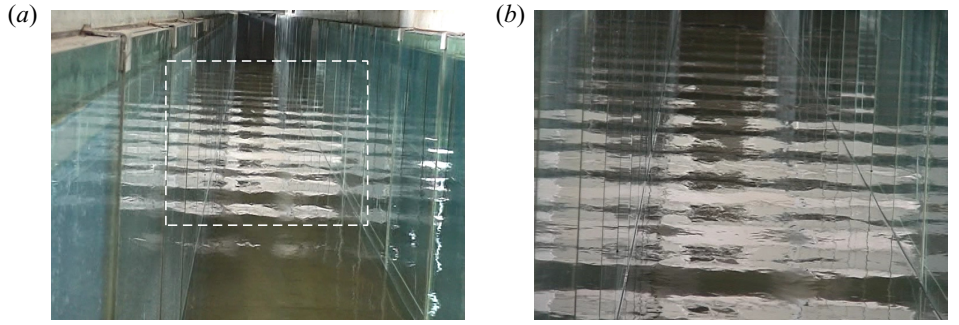

Figure 12. Instantaneous free-surface pattern upstream of the rippled bottom, showing the presence of upstream-propagating waves for the experimental case in figure 11. (*b*) Close-up of the enclosed region in panel (*a*).

show that the upstream-propagating waves with significantly large amplitude exist only in the narrow critical range of current speed for a given ripple configuration and water depth. The amplitude of the unsteady wave is negligibly small away from the critical range of current speed. For given ripple steepness, the critical current speed is observed to increase as the water depth decreases. For given water depth, the critical current speed is seen to decrease as the ripple steepness increases. The wave generation phenomenon becomes weaker at larger water depth in general. The upper limit of water depth for the observed wave generation becomes larger with steeper bottom ripples.

Figure 14 depicts the period of upstream-propagating waves as a function of current speed for different bottom steepnesses and water depths. The results indicate that the period of the upstream-propagating waves is in the narrow range of 1.2 s to 1.5 s. The wave period generally becomes larger with increasing current speed except at very shallow water depth and steep bottom ripples, under which the wave motion over the rippled area is strongly nonlinear.

Figure 15 displays the spatial variation of the generated unsteady wave amplitude over the rippled bottom patch as well as upstream of the patch. In this figure, only representative

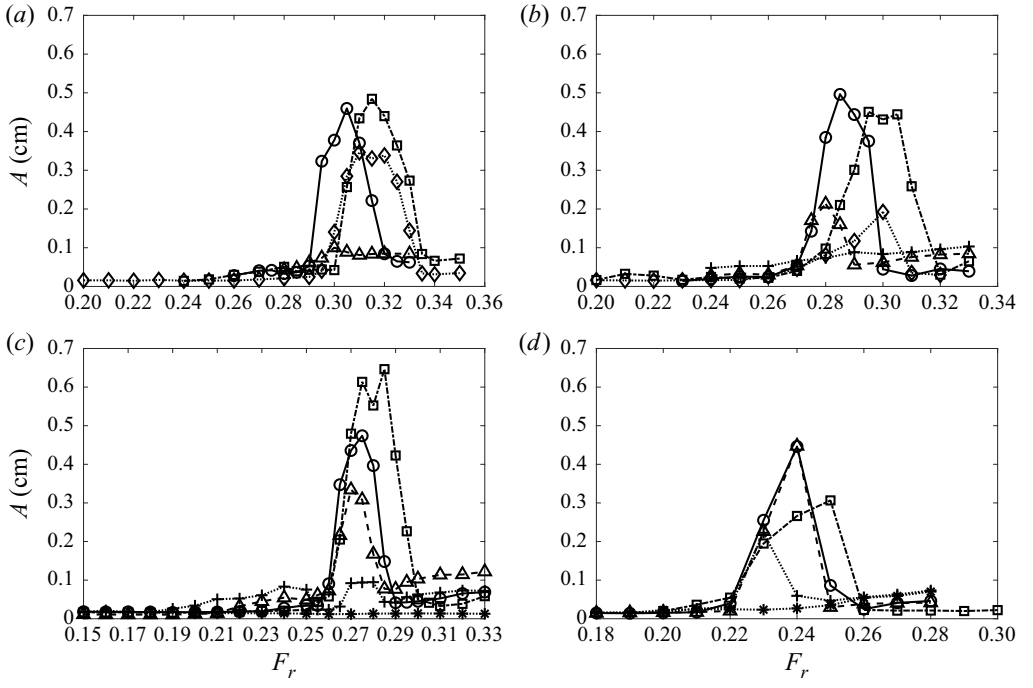

Figure 13. Experimental data of the amplitude of upstream-propagating waves (over the upstream flat bottom) as a function of the Froude number (F_r) for the bottom ripple steepness (*a*) $\epsilon_b = 0.602$, (*b*) 0.694, (*c*) 0.798 and (*d*) 1.047 with water depth $h/\lambda_b = 0.5$ (⋄), 0.6 (□), 0.7 (○), 0.8 (△), 0.9 (+) and 1.0 (∗).

cases are plotted for clarity. For all the cases shown, the unsteady wave amplitude increases rapidly from a near-zero value with distance from the downstream edge of the rippled bottom and reaches a peak value at approximately one to two ripple wavelengths from the upstream edge of the rippled bottom, and then reduces to a near-constant value over the flat upstream bottom. The unsteady wave amplitude is seen to be negligibly small over the downstream flat bottom.

Apart from the wave amplitude, we show in figure 16 the spatial variation of the primary unsteady wave period over the rippled bottom patch for some representative cases. The experimental data indicates that the periods of the generated (dominant) unsteady wave components in all cases remain nearly invariant over the entire rippled bottom. We note that, in the case of very shallow depth and steep ripples, super-harmonic (double-frequency) wave components are also observed due to strong nonlinear free-surface boundary effects.

6. Comparison between theory and experiment

In this section, we quantitatively compare the theoretical prediction with the experimental data for the condition under which the upstream-propagating waves are produced when a steady current passes over a rippled bottom patch. The spatial variation of the generated unsteady wave amplitude by the theory is qualitatively compared with the experimental measurements. The possible reasons causing the discrepancy between the theoretical prediction and experimental data are discussed.

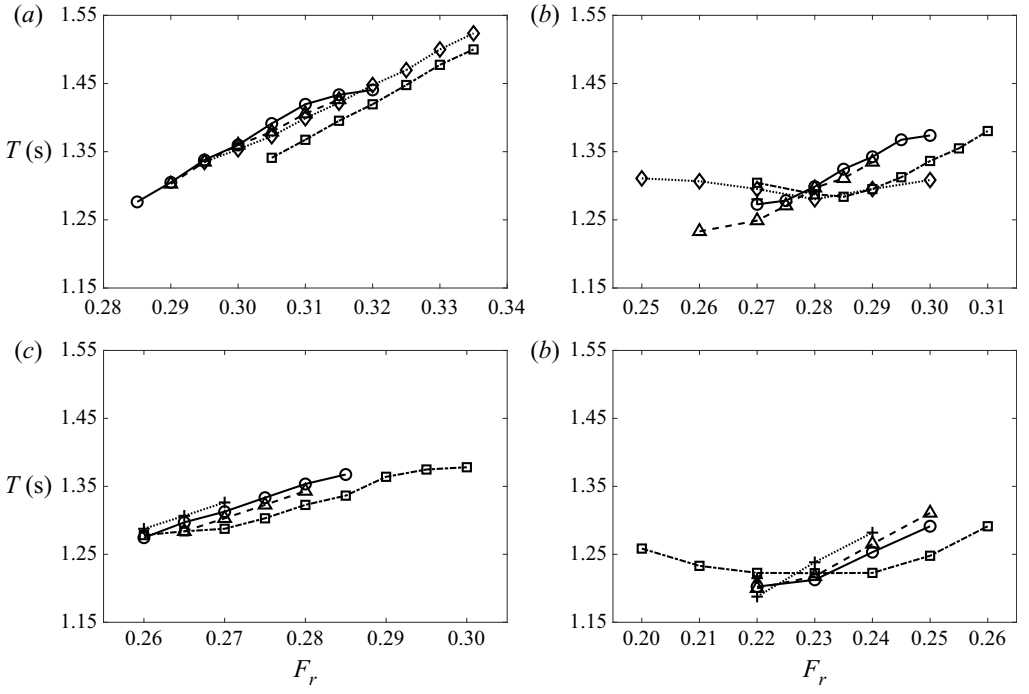

Figure 14. Experimental data of the period of upstream-propagating waves (over the upstream flat bottom) as a function of the Froude number (F_r) for the bottom ripple steepness (*a*) $\epsilon_b = 0.602$, (*b*) 0.694, (*c*) 0.798 and (*d*) 1.047 with water depth $h/\lambda_b = 0.5$ ($\diamond$), 0.6 ($\square$), 0.7 ($\circ$), 0.8 ($\triangle$), 0.9 ($+$) and 1.0 ($*$).

6.1. *Period of generated upstream-propagating wave versus current speed*

As discussed in § 3, resonant triads (1), (5) and (6) all involve the upstream-propagating (k_1) wave component. Among them, triad (5) can be excluded since the steady flow is spatially stable to small unsteady wave disturbances that are contained in triad (5) (see table 2). In principle, triads (1) and (6) could produce the k_1 wave component. The experimental data of the observed k_1 wave period, however, clearly exclude the possible participation of triad (1). We thus compare the theory with experiments for triad (6) only.

We first compare the frequency and wavenumber of the unsteady wave measured at the upstream side of the rippled bottom patch in the flume with the theoretical prediction from the resonance condition of triad (6). For the experimental data, the wave frequency is chosen to be the peak frequency of the free-surface elevation spectrum. The wavenumber is calculated from its relation with the frequency and phase speed. The phase speed of the wave can be determined from the correlation coefficient of the wave elevation measured at two neighbouring wave gauges (Kyotoh & Fukushima 1997).

In figures 17–21, we present the experimental data of the frequency of the observed upstream-propagating waves versus the associated incoming current speed with different ripple steepnesses and water depths. In relatively deep depth ($h/\lambda_b = 0.9$), the data for the mildest ripple case ($\epsilon_b = 0.602$) are not shown in figure 17 since the amplitude of the upstream-propagating wave is negligibly small. In the shallow depth ($h/\lambda_b = 0.5$), the data for the steep ripple cases ($\epsilon_b = 0.798$ and 1.047) are not shown in figure 21 since the flow motion is strongly nonlinear and turbulent. In these figures, the theoretical condition for the resonant triad (6), expressed as the relation between the frequency of the upstream-propagating wave and the incoming current speed, is also shown for comparison

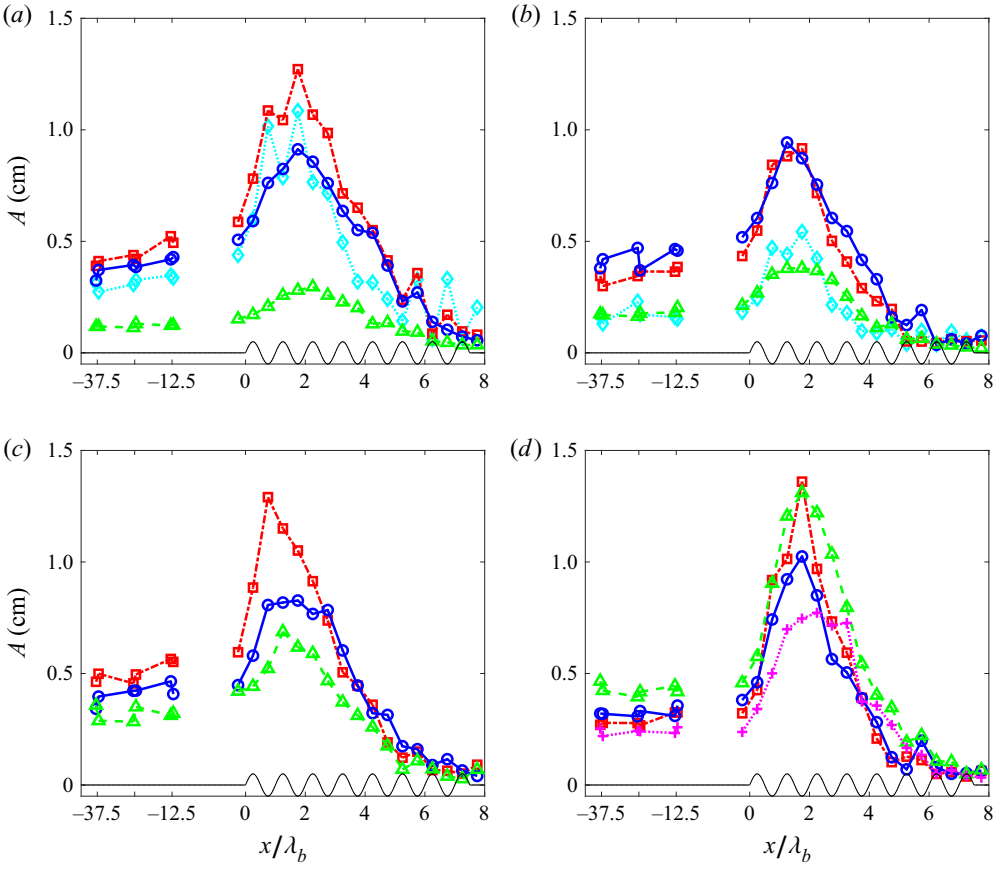

Figure 15. Experimental data of the spatial variation of the unsteady wave amplitude over the rippled bottom and upstream flat bottom with: (*a*) $\epsilon_b = 0.602$ for $h/\lambda_b = 0.5$ and $F_r = 0.320$ (◇), $h/\lambda_b = 0.6$ and $F_r = 0.315$ (□), $h/\lambda_b = 0.7$ and $F_r = 0.305$ (○) and $h/\lambda_b = 0.8$ and $F_r = 0.300$ (△); (*b*) $\epsilon_b = 0.694$ for $h/\lambda_b = 0.5$ and $F_r = 0.300$ (◇), $h/\lambda_b = 0.6$ and $F_r = 0.305$ (□), $h/\lambda_b = 0.7$ and $F_r = 0.285$ (○) and $h/\lambda_b = 0.8$ and $F_r = 0.285$ (△); (*c*) $\epsilon_b = 0.798$ for $h/\lambda_b = 0.6$ and $F_r = 0.280$ (□), $h/\lambda_b = 0.7$ and $F_r = 0.275$ (○) and $h/\lambda_b = 0.8$ and $F_r = 0.270$ (△); and (*d*) $\epsilon_b = 1.047$ for $h/\lambda_b = 0.6$ and $F_r = 0.250$ (□), $h/\lambda_b = 0.7$ and $F_r = 0.240$ (○), $h/\lambda_b = 0.8$ and $F_r = 0.240$ (△) and $h/\lambda_b = 0.9$ and $F_r = 0.230$ (+). (Note that the horizontal scale over the flat bottom for $x < 0$ differs from that over the rippled bottom for $x \geqslant 0$.)

with the experimental data. The comparisons show that, in the cases with relatively mild ripples and large water depths, the experimental data fall right on or very close to the theoretical curves. In the cases with steeper ripples and shallow water depths, the experimental data somewhat shift from the theoretical curves to the lower current speeds. The discrepancy between the experimental data and the theoretical prediction becomes larger as the ripple steepness increases and/or water depth decreases. We note that the theory assumes a uniform incoming current while the experimental data use the average flow velocity, which is equal to the flow flux divided by the mean water depth over the flat bottom. Owing to the real-fluid effect in the experiments, the flow velocity near the free surface is known to be larger in magnitude than the average velocity. This effect is stronger for shallower depth. After taking this fact into account, the experimental data would move towards larger current speeds, leading to better agreement with the theory than appeared in figures 17–21.

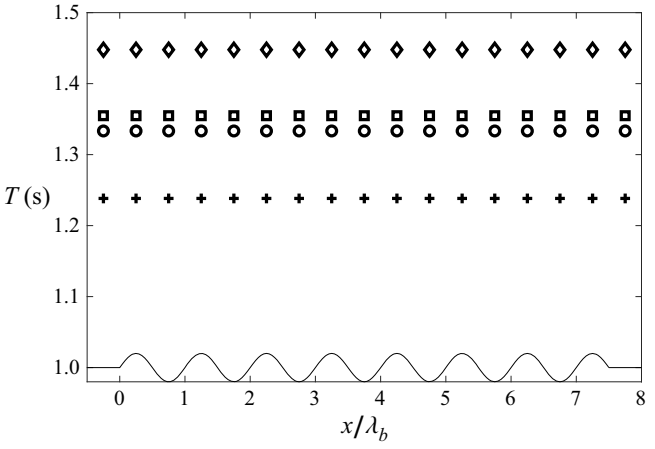

Figure 16. Experimental data of the spatial variation of the primary unsteady wave period over the rippled bottom with: $\epsilon_b = 0.602$, $h/\lambda_b = 0.5$ and $F_r = 0.320$ (◇); $\epsilon_b = 0.694$, $h/\lambda_b = 0.6$ and $F_r = 0.305$ (□); $\epsilon_b = 0.798$, $h/\lambda_b = 0.7$ and $F_r = 0.275$ (○); and $\epsilon_b = 1.047$, $h/\lambda_b = 0.9$ and $F_r = 0.230$ (+).

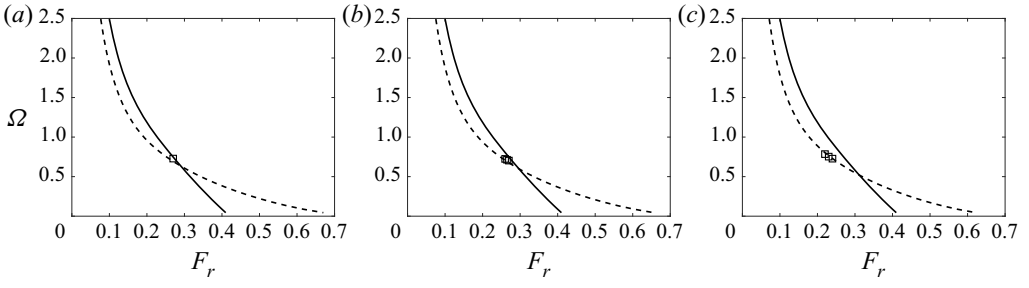

Figure 17. Comparison of the frequency ($\Omega = \omega(h/g)^{1/2}$) of the triad-resonance-generated upstream-propagating wave as a function of current speed ($F_r = U/(gh)^{1/2}$) between the experimental measurements (□) and the theoretical prediction from the resonance condition for triad (6) (——) in the case of water depth $h/\lambda_b = 0.9$ and bottom ripple steepness (*a*) $\epsilon_b = 0.694$, (*b*) 0.798 and (*c*) 1.047. The critical flow condition over the rippled bottom region (- - -) is shown for reference.

Figure 22 shows the comparisons of the wavenumber of the upstream-propagating waves as a function of the current speed between the experimental measurements and the theoretical prediction from the resonance condition for triad (6). Consistent with the frequency comparisons shown in figures 17–21, better agreements between the experimental data and the theoretical prediction are obtained for the cases with mild bottom ripples and/or relatively large water depths. As discussed above, if the real-fluid effect on the surface current speed is accounted for, the experimental data in the cases of steep bottom ripples and shallow water depth would be moved to larger values of F_r, leading to better agreements with the theory.

The good agreements between the experimental data and the theory on the kinematics of the upstream-propagating waves confirm that the triad resonance involving the unsteady k_1 and k_2 waves as well as stationary bottom ripples (and/or the resulting steady waves) is capable of producing upstream-propagating waves (i.e. with wavenumber k_1) when a steady current passes over a rippled bottom patch. The remaining question is why the generation of upstream-propagating waves in the experiment is clearly observed only in a

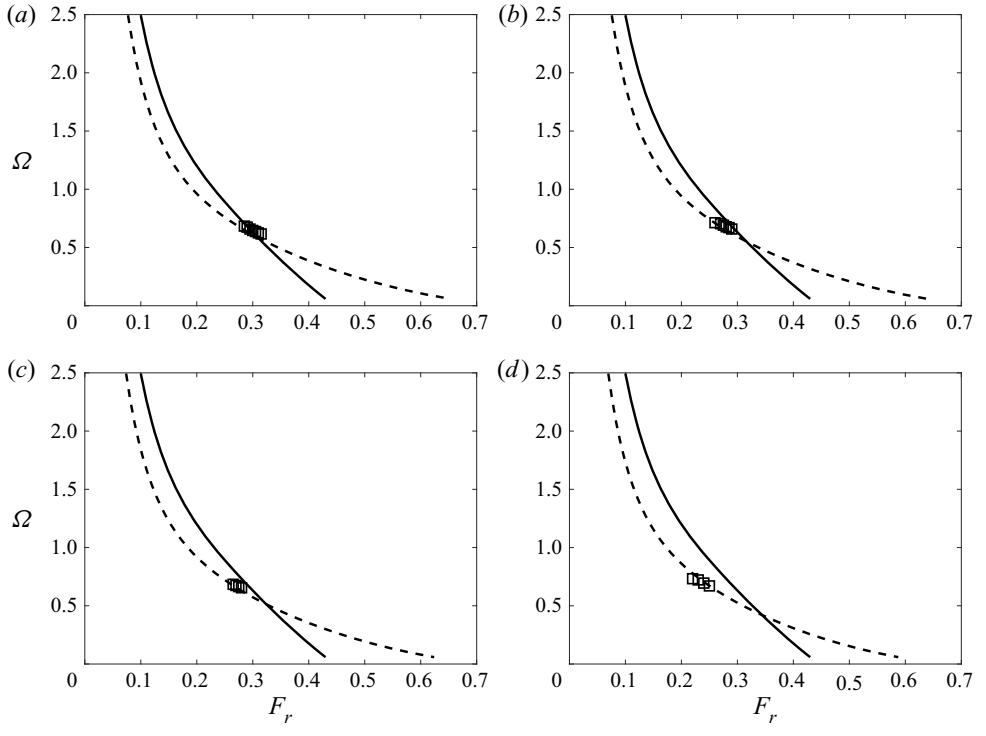

Figure 18. Comparison of the frequency ($\Omega = \omega(h/g)^{1/2}$) of the triad-resonance-generated upstream-propagating wave as a function of current speed ($F_r = U/(gh)^{1/2}$) between the experimental measurements (□) and the theoretical prediction from the resonance condition for triad (6) (——) in the case of water depth $h/\lambda_b = 0.8$ and bottom ripple steepness (*a*) $\epsilon_b = 0.602$, (*b*) 0.694, (*c*) 0.798 and (*d*) 1.047. The critical flow condition over the rippled bottom region (- - -) is shown for reference.

narrow range of current speeds but not for speeds outside this critical range, for which the same type of triad resonances can also occur in theory.

The analysis in § 4.3 indicates that the amplitude of the upstream-propagating wave can be significantly amplified if the triad resonance happens in the neighbourhood of the critical wave-flow condition (described in terms of critical current speed U_c and critical wave frequency ω_c). Note that ω_c is uniquely related to U_c as shown in figure 2(*b*). To examine the role of the critical wave flow on the upstream-propagating wave generation in the experiments, we need to estimate the (near-surface) current speed over the rippled bottom patch where the triad resonant wave–ripple interactions occur. The average current speed over the rippled bottom patch ($\tilde{U}$) is actually larger than the ideal uniform current speed (U) (used in the theoretical analysis) due to two factors associated with the real-fluid effects in the flow over bottom ripples.

First, it is known from the existing numerical and experimental studies in the literature that, when a uniform incoming flow passes over a sinusoidal rippled solid surface, flow separation occurs in the case of relatively large ripple amplitudes (Zilker & Hanratty 1979; Buckles, Hanratty & Adrian 1984; Kuzan, Hanratty & Adrian 1989; Hudson, Dykhno & Hanratty 1996; Shen *et al.* 2003). Since the time-averaged flow velocity in the separated-flow region on the leeward side of ripples is much smaller than outside the separated-flow region (Buckles *et al.* 1984), it is reasonable (and in fact conservative) to assume that the effective depth over which the flow fluxes downstream is the distance from

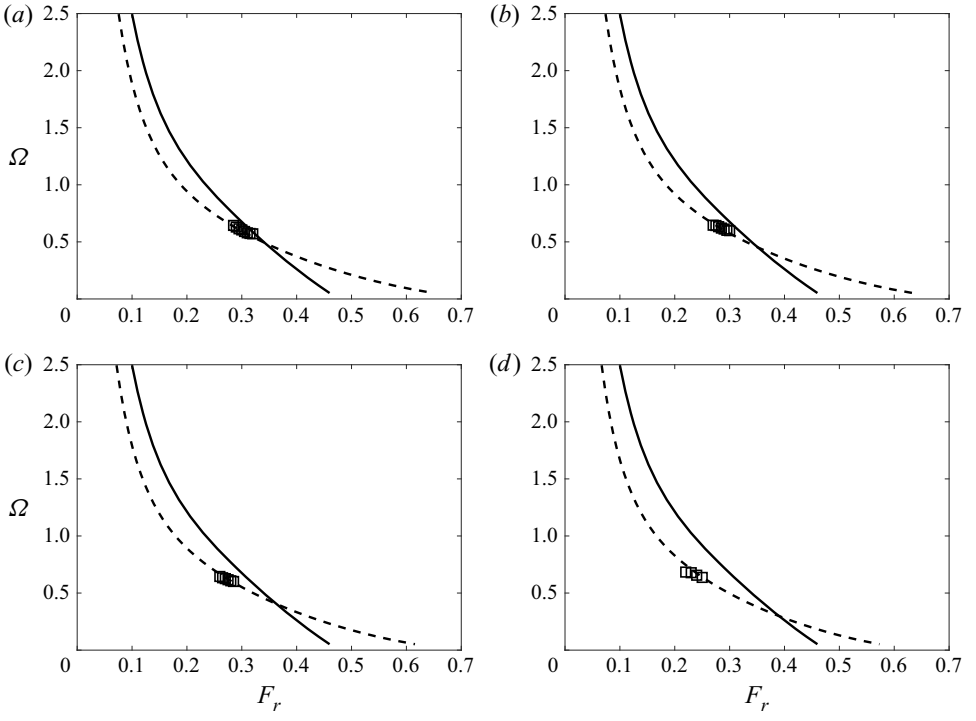

Figure 19. Comparison of the frequency ($\Omega = \omega(h/g)^{1/2}$) of the triad-resonance-generated upstream-propagating wave as a function of current speed ($F_r = U/(gh)^{1/2}$) between the experimental measurements (□) and the theoretical prediction from the resonance condition for triad (6) (——) in the case of water depth $h/\lambda_b = 0.7$ and bottom ripple steepness (*a*) $\epsilon_b = 0.602$, (*b*) 0.694, (*c*) 0.798 and (*d*) 1.047. The critical flow condition over the rippled bottom region (- - -) is shown for reference.

the crest of the ripples to the mean water surface, $h - b$. This would enlarge $\tilde{U}$ from U by a factor of $\xi_1 = h/(h - b)$.

Second, the incoming current in the flume is actually a shear flow over the stationary flat bottom so that the flow velocity near the free surface is larger than the depth-averaged speed U. Figure 23 shows the experimental data of two sample vertical profiles of steady current in the flume of a flat bottom. The approximate velocity profiles from the empirical 1/7th and 1/11th power laws for the fully developed boundary layers are also shown for comparison. At relatively large water depth with smaller velocity, the velocity profile is seen to match the 1/7th power law well. At shallow depth with larger velocity, the velocity profile is better described by the $1/n$th power law with $n > 7$, which is consistent with the finding in the literature (Schlichting & Gersten 2017). For illustration, based on the empirical 1/7th power law (White 2006), we obtain the displacement thickness $\delta^* = h/8$. This effect would further enlarge $\tilde{U}$ from U by a factor of $\xi_2 = h/(h - \delta^*) = 1.143$. Upon combining these two real-fluid effects, we have the relation $\tilde{U} = \xi_1\xi_2 U$.

In figures 17–21, we plot the critical wave-flow condition over the rippled bottom patch, which is represented by the dashed line. We note that the theoretical resonance condition for triad (6) and the experimental data points in these figures are displayed in terms of the ideal (depth-averaged) uniform current velocity U (i.e. $F_r = U/(gh)^{1/2}$). Thus, any point on this dashed line represents that the wave flow over the rippled bottom has the critical wave frequency (ω_c) and critical current speed $\tilde{U}_c$, while the corresponding uniform flow

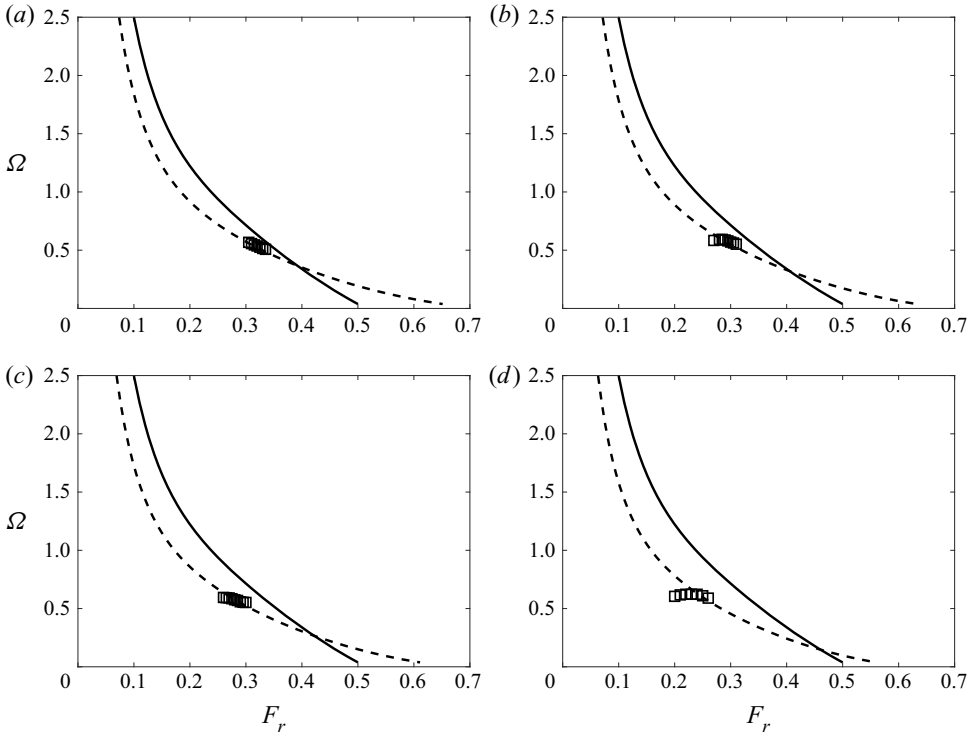

Figure 20. Comparison of the frequency ($\Omega = \omega(h/g)^{1/2}$) of the triad-resonance-generated upstream-propagating wave as a function of current speed ($F_r = U/(gh)^{1/2}$) between the experimental measurements (□) and the theoretical prediction from the resonance condition for triad (6) (——) in the case of water depth $h/\lambda_b = 0.6$ and bottom ripple steepness (*a*) $\epsilon_b = 0.602$, (*b*) 0.694, (*c*) 0.798 and (*d*) 1.047. The critical flow condition over the rippled bottom region (- - -) is shown for reference.

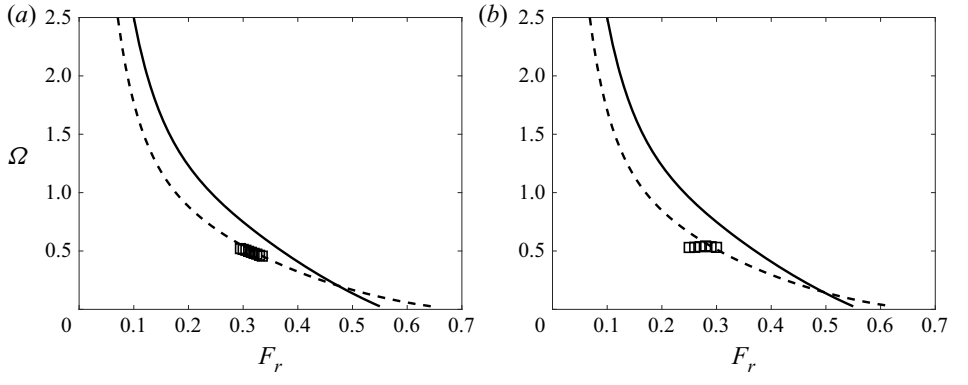

Figure 21. Comparison of the frequency ($\Omega = \omega(h/g)^{1/2}$) of the triad-resonance-generated upstream-propagating wave as a function of current speed ($F_r = U/(gh)^{1/2}$) between the experimental measurements (□) and the theoretical prediction from the resonance condition for triad (6) (——) in the case of water depth $h/\lambda_b = 0.5$ and bottom ripple steepness (*a*) $\epsilon_b = 0.602$ and (*b*) 0.694. The critical flow condition over the rippled bottom region (- - -) is shown for reference.

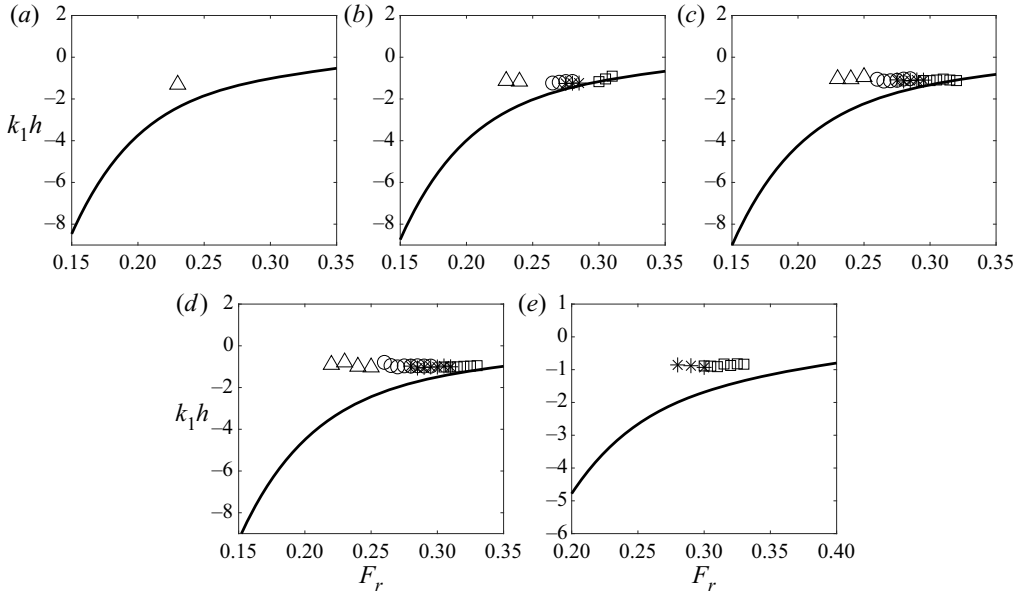

Figure 22. Comparison of the wavenumber (k_1h) of the triad-resonance-generated upstream-propagating wave as a function of current speed ($F_r = U/(gh)^{1/2}$) between the theoretical prediction from the resonance condition for triad (6) (——) and the experimental measurements with bottom ripple steepness $\epsilon_b = 0.602$ (□), 0.694 (∗), 0.798 (○) and 1.047 (△) and water depth (*a*) $h/\lambda_b = 0.9$, (*b*) 0.8, (*c*) 0.7, (*d*) 0.6 and (*e*) 0.5.

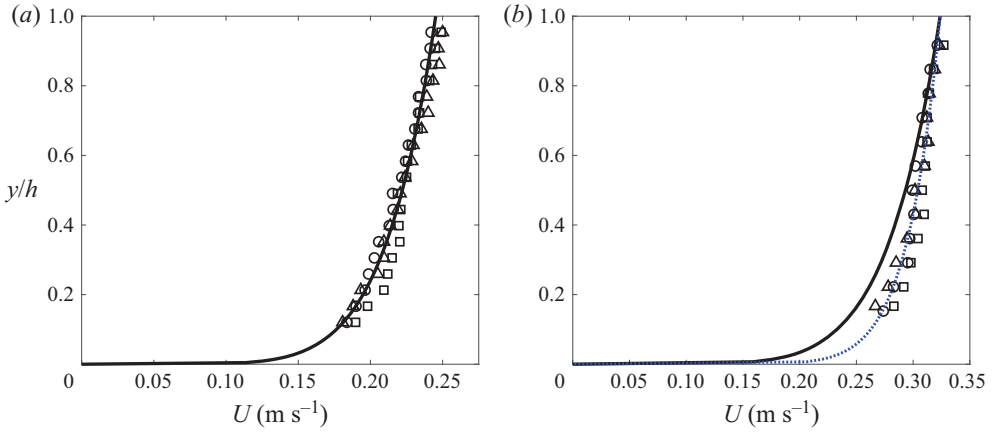

Figure 23. Vertical profiles of horizontal velocity of the steady current in the flume with a flat bottom with water depth (*a*) $h/\lambda_b = 0.9$ and (*b*) 0.6, where $\lambda_b = 0.24$ m. The symbols and curves represent the experimental data from velocity gauges A (△), B (□) and C (○) as well as the approximate velocity profiles from the 1/7th (——) and 1/11th (· · · · · ·) power laws. (Gauges A, B and C are located at 1.5 m, 0.9 m and 0.3 m from the upstream edge of the ripple patch.)

speed over the flat bottom is given by $U = \tilde{U}_c/(\xi_1\xi_2)$. We see in figures 17–21 that the experimental data points are clustered in the close neighbourhood of the intersection of the critical wave-flow curve and the triad resonance condition curve. In particular, the experimental data points are seen to be right at this intersection point in the cases with mild ripples and large water depths. This shows that the observable upstream-propagating waves

(with a significantly large amplitude) are generated by the triad resonant wave–ripple interactions only when the wave flow over the rippled bottom region is near the critical condition associated with wave frequency ω_c and current speed $\tilde{U}_c$. For steeper ripples at shallower water depth, the experimental data points are seen to slightly deviate from this intersection point to lower current speed. This deviation may be due to several factors. First, as mentioned above, since the experimental data points are plotted in terms of the uniform depth-averaged flow speed U, they are shifted to somewhat lower speed due to the shear flow effect. Second, the flow separation effect near the rippled bottom is underestimated by the use of ξ_1, especially at relatively shallow depth and steeper ripples. Third, nonlinear ripple amplitude effects on the wave dispersion relation could influence the theoretical prediction of the triad resonance condition (which is based on the linear dispersion relation in the present study). Detailed understanding and quantification of these real-fluid and higher-order nonlinear effects requires the use of expensive turbulent flow computations, which is beyond the scope of this work.

Away from the neighbourhood of the intersection point, the triad resonant wave–ripple interaction still occurs, but with the growth rate $\theta = O(1)$ (i.e. bounded). In this case, as the analysis in § 4.3 shows, the maximum amplitude of the generated upstream-propagating wave depends on the length (L) of the rippled bottom patch. As a result, the generated upstream-propagating waves may not be observable in the physical experiments if L is not sufficiently large. This is consistent with the feature of comparisons between the experiment and the present theory in figures 17–21.

6.2. *Spatial variation of upstream-propagating wave amplitude*

The theoretical analysis in § 4.3 provides an asymptotic solution of the amplitudes, (4.8*a*,*b*), of the interacting waves involved in the triad resonance or near-resonance. For given bottom ripple properties and water depth, the current speed ($\tilde{U}$) over the rippled bottom patch and the amplitude of the k_2 wave (a_2) at the starting location ($x = L$) of resonant wave–ripple interactions are needed to evaluate the theoretical solution of $A_1(x)$ and $A_2(x)$. To compare the theoretical prediction with the experimental measurements, we let a_2 be the small experimental value of the unsteady wave amplitude at $x = L$. To determine $\tilde{U}$, we match the theoretical solution of the (maximum) unsteady wave amplitude $|A_1(x) + A_2(x)|$ to the experimental data.

Figure 24 displays representative comparisons of the theoretical solution of $|A_1(x) + A_2(x)|$, given by (4.8*a*,*b*), with the experimental data for two sample cases with (*a*) $\epsilon_b = 0.602$, $h/\lambda_b = 0.8$ and $F_r = 0.30$ and (*b*) $\epsilon_b = 0.694$, $h/\lambda_b = 0.7$ and $F_r = 0.285$, respectively. For the theoretical solution, $\tilde{U} = 0.994U_c$ and $\tilde{U} = 0.985U_c$ are used in cases (*a*) and (*b*), respectively. It is seen that the theoretical prediction agrees with the experimental data very well over most of the rippled bottom patch (for $(2\text{–}2.5)\lambda_b \leqslant x \leqslant L$), in particular, on the feature of exponential growth of $A_{1,2}(x)$ with the interaction distance from the starting point ($L - x$). In the upstream end region of the rippled patch ($0 \leqslant x < (2\text{–}2.5)\lambda_b$), unlike the theoretical solution, the experimental data show that $|A_1(x) + A_2(x)|$ reverses the trend of exponential growth with $L - x$ and reduces to a value that matches the amplitude of upstream-propagating waves over the flat bottom. The reason for the deviation of the experimental data from the theoretical prediction (4.8*a*,*b*) is that, in the experiment, the current speed U over the upstream flat bottom is slightly smaller than $\tilde{U}$ over the rippled patch so that A_2 must decrease to vanish at $x = 0$ since the k_2 wave cannot exist in the upstream flat bottom. This would reduce the

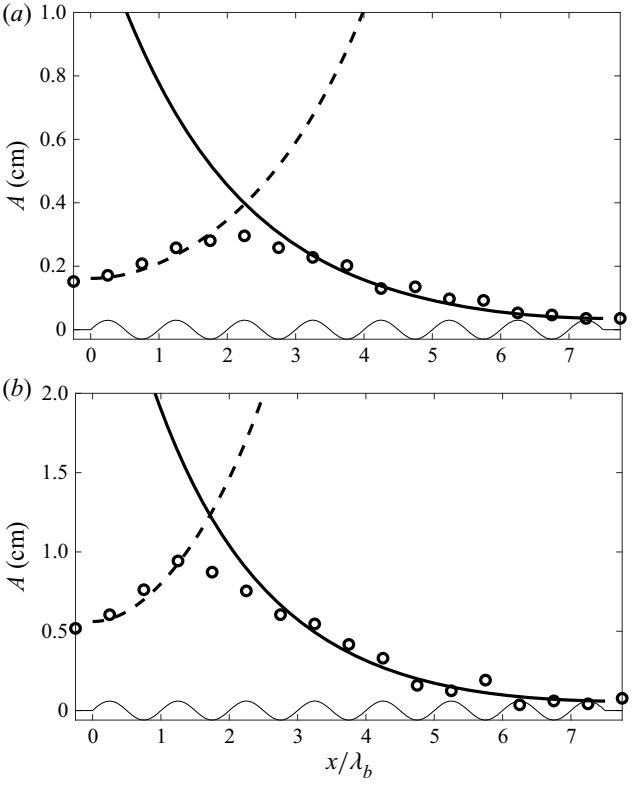

Figure 24. Comparison of the amplitude of unsteady waves, $|A_1(x) + A_2(x)|$, over the rippled bottom patch between the experimental measurement (○) and the theoretical solutions (4.8*a*,*b*) (——) and (6.1*a*,*b*) (- - -) for: (*a*) $\epsilon_b = 0.602$, $h/\lambda_b = 0.8$ and $F_r = 0.30$; and (*b*) $\epsilon_b = 0.694$, $h/\lambda_b = 0.7$ and $F_r = 0.285$.

growth of $A_1(x)$ by the triad resonance in the region near the upstream end of the rippled bottom patch. This effect is, however, not considered in the theoretical solution (4.8*a*,*b*), which is determined based on the boundary conditions at the downstream end only.

While it is an uneasy analytical practice to derive the theoretical solution that accounts for the varying current speed effect over the entire rippled bottom patch, we can obtain an asymptotic solution in the upstream end region of the rippled patch, which is controlled by the boundary conditions at $x = 0$. We consider the boundary conditions: $A_2(x = 0) = 0$ and $A_1(x = 0) = a_1$, with a_1 being equal to the experimental measurement of the unsteady wave amplitude at $x = 0$. From (4.2), we obtain the slope condition: $\mathrm{d}A_1/\mathrm{d}x(x = 0) = 0$ and $\mathrm{d}A_2/\mathrm{d}x(x = 0) = \mathrm{i}a_1\mathbb{Q}/C_2$. With these boundary conditions, we solve (4.7) for $A_1(x)$ and $A_2(x)$ to obtain:

$$A_1(x) = a_1 \cosh(\theta x) \quad \text{and} \quad A_2(x) = \mathrm{i}a_1 \frac{\mathbb{Q}}{\theta C_2} \sinh(\theta x). \tag{6.1a,b}$$

For comparison, these solutions (with $\tilde{U} = 0.994U_c$ and $0.985U_c$, respectively, for cases (*a*) and (*b*)) are also presented in figure 24. It is seen that the theoretical solution (6.1*a*,*b*) matches the experimental data quite well in the upstream end region of the rippled patch ($0 \leqslant x < (1.5\text{–}2)\lambda_b$). Together, the theoretical solutions (4.8*a*,*b*) and (6.1*a*,*b*) properly reflect the distinctive growth feature of the unsteady waves by near-triad resonance over the rippled bottom patch observed in the experiment. In addition, the results of $\tilde{U} = 0.994U_c$

and $0.985U_c$ in these two sample cases further confirm that the significant development of the upstream-propagating wave can be achieved only when the associated triad resonance occurs near the critical wave-flow condition over the rippled bottom.

7. Concluding remarks

We study the generation mechanism governing the formation of upstream-propagating waves in a steady current that passes over a horizontal bottom with a patch of sinusoidal ripples by the use of multiple-scale perturbation analyses and laboratory experiments. In the context of potential flow assumptions, we examine the role of triad resonances involving two unsteady wave components of the same frequency and one bottom ripple (or steady wave) component in the presence of a uniform current. We identify the conditions and their parametric domains of existence for six possible triads that can form second-order resonant wave–ripple interactions. We derive the amplitude evolution equations of interacting waves in the resonant triad, from which we deduce the temporal and spatial stabilities of the steady flow over an infinitely extended rippled bottom. We show that the triad resonant or near-resonant interactions in a steady flow over a finite rippled bottom patch can generate unsteady waves that propagate upstream against the incoming current. In particular, we find that the generation of upstream-propagating waves can be dramatically amplified when the triad resonance (or near-resonance) occurs in the neighbourhood of the critical wave-flow condition under which the group velocities of the generated waves are near zero over the rippled bottom. This phenomenon is associated with the spatial instability of the flow, which cannot be found from the temporal instability analysis.

To verify and assist in understanding the theory, we conduct a series of laboratory experiments in a relatively large-scale flume to observe the development of upstream-propagating waves for wide ranges of ripple steepnesses, water depths and current speeds. The frequency and amplitude of the induced unsteady waves along the flume are acquired. It is observed that, for given rippled bottom configuration and water depth, measurable upstream-propagating waves are produced only when the current reaches a narrow range of critical speed. For given ripple wavenumber, the critical current speed generally becomes smaller while the frequency of the upstream-propagating waves is slightly larger for shallower water depth and/or steeper ripple steepness. The comparisons between the flume experiments and the theoretical analyses show that the frequency and wavenumber of the upstream-propagating waves observed in the experiments match the theoretical prediction based on the triad resonance condition, $k_1 - k_2 = k_b$, where k_1 is the wavenumber of the upstream-propagating wave (with negative phase and group velocities), k_2 is the wavenumber of the unsteady wave whose phase/group velocity is negative/positive, and k_b is the ripple wavenumber. The comparisons also show that the upstream-propagating waves with appreciable amount of energy, which are observable in the experiments, can be generated only when the associated triad resonance happens near the critical wave-flow condition under which the k_1 and k_2 waves have near-zero group velocities. This is due to the fact that, near the critical wave-flow condition, the k_1 and k_2 waves can be significantly developed by taking energy from the current through the triad resonant or near-resonant wave–ripple interactions over the rippled bottom region and the k_1 wave can then propagate upstream over the flat bottom since the current speed over the flat bottom is slightly less than the critical velocity over the rippled bottom (due to real-fluid effects). Consistent with this understanding, the spatial variation of the generated unsteady waves over the rippled bottom predicted by the theory compares well with the experimental measurements.

We finally remark that the agreement between the theoretical prediction and the laboratory measurements on the flow condition for the observation of induced upstream-propagating waves becomes poorer in the cases of steep bottom ripples and shallow water depths, in which the higher-order wave–ripple interactions and real-fluid effects may play a more important role. To better understand such effects, it is necessary to adopt simulations based on the Navier–Stokes equations, which are currently being pursued.

Acknowledgements. All major data are included in the paper. Additional raw experimental data can be obtained from the authors, J.F. (fanjun@hhu.edu.cn) or J.Z. (jhzheng@hhu.edu.cn).

Funding. This research was supported by the National Natural Science Foundation of China (Grant no. U1706230) and the National Science Fund for Distinguished Young Scholars (Grant no. 51425901).

Declaration of interests. The authors report no conflict of interest.

Author ORCIDs.
Jun Fan http://orcid.org/0000-0002-7322-2398;
Yuming Liu http://orcid.org/0000-0003-2238-364X.

Appendix A. Derivation of amplitude evolution equations of interacting waves in a resonant triad

We apply the multiple-scale perturbation analysis to derive the spatio-temporal evolution equations for the amplitudes of interacting waves in a resonant triad under the general resonance condition (3.1*a*,*b*). Upon introducing the slowly varying spatial and temporal coordinate $\bar{x} = \epsilon x$ and $\bar{t} = \epsilon t$ and expanding the velocity potential and free-surface elevation in perturbation series with respect to the small parameter $\epsilon \ll 1$, we obtain

$$\phi(x, z, t, \bar{x}, \bar{t}) = \epsilon\phi^{(1)}(x, z, t, \bar{x}, \bar{t}) + \epsilon^2\phi^{(2)}(x, z, t, \bar{x}, \bar{t}) + \cdots \tag{A1}$$

and

$$\eta(x, t, \bar{x}, \bar{t}) = \epsilon\eta^{(1)}(x, t, \bar{x}, \bar{t}) + \epsilon^2\eta^{(2)}(x, t, \bar{x}, \bar{t}) + \cdots, \tag{A2}$$

where $(\,)^{(m)} = O(1)$, $m = 1, 2, \ldots$, with the superscript m denoting the coefficient of the mth-order quantity. Substituting the expansions in (A1) and (A2) into the nonlinear BVP, (2.2)–(2.5), for the wave motion in the presence of a uniform current and expanding the boundary conditions on the instantaneous free surface (and exact bottom) in Taylor series with respect to the mean free surface $z = 0$ (and the mean bottom $z = -h$), we have the field equation

$$\epsilon[\phi^{(1)}_{xx} + \phi^{(1)}_{zz}] + \epsilon^2[\phi^{(2)}_{xx} + 2\phi^{(1)}_{\bar{x}x} + \phi^{(2)}_{zz}] + \text{H.O.T.} = 0, \quad -h \leqslant z \leqslant 0, \tag{A3}$$

where 'H.O.T.' denotes higher than second-order terms, the free-surface kinematic boundary condition

$$\epsilon[\eta^{(1)}_t + U\eta^{(1)}_x - \phi^{(1)}_z] + \epsilon^2[\eta^{(2)}_t + \eta^{(1)}_{\bar{t}} + U\eta^{(2)}_x + U\eta^{(1)}_{\bar{x}} + \phi^{(1)}_x\eta^{(1)}_x - \phi^{(2)}_z - \eta^{(1)}\phi^{(1)}_{zz}] + \text{H.O.T.} = 0, \quad z = 0, \tag{A4}$$

the free-surface dynamic boundary condition

$$\epsilon[\phi^{(1)}_t + U\phi^{(1)}_x + g\eta^{(1)}] + \epsilon^2[\phi^{(2)}_t + \phi^{(1)}_{\bar{t}} + \eta^{(1)}\phi^{(1)}_{tz} + \tfrac{1}{2}\phi^{(1)}_x\phi^{(1)}_x + U\phi^{(2)}_x + U\phi^{(1)}_{\bar{x}} + U\eta^{(1)}\phi^{(1)}_{xz} + \tfrac{1}{2}\phi^{(1)}_z\phi^{(1)}_z + g\eta^{(2)}] + \text{H.O.T.} = 0, \quad z = 0, \tag{A5}$$

and the bottom boundary condition

$$\epsilon(\phi_z^{(1)} - \zeta_x U) + \epsilon^2(\phi_z^{(2)} + \zeta\phi_{zz}^{(1)} - \phi_x^{(1)}\zeta_x) + \text{H.O.T.} = 0, \quad z = -h. \tag{A6}$$

A.1. *First-order problem*

From (A3) to (A6), we obtain the first-order BVP for $\phi^{(1)}$,

$$\left.\begin{aligned} \phi_{xx}^{(1)} + \phi_{zz}^{(1)} &= 0, \quad -h \leqslant z \leqslant 0, \\ \phi_{tt}^{(1)} + 2U\phi_{xt}^{(1)} + U^2\phi_{xx}^{(1)} + g\phi_z^{(1)} &= 0, \quad z = 0, \\ \phi_z^{(1)} &= U\zeta_x, \quad z = -h, \end{aligned}\right\} \tag{A7}$$

and the first-order wave elevation $\eta^{(1)}$ given in terms of $\phi^{(1)}$,

$$\eta^{(1)} = -\frac{1}{g}\left[\phi_t^{(1)} + U\phi_x^{(1)}\right]_{z=0}. \tag{A8}$$

For the purpose of understanding the development of unsteady waves by taking energy from the steady flow through a triad resonance, we consider the wave field consisting of two unsteady wave components (with wavenumbers k_m and k_n) and one stationary wave component that results from the steady problem of current interaction with bottom ripples (with wavenumber k_b). From the resonance condition (3.1*a*,*b*), we have $k_m - k_n = k_b$ and $\omega_m = \omega_n$ ($\equiv \omega$). The associated first-order velocity potential of the wave field takes the form in (4.1). The free-surface elevation is given by

$$\begin{aligned} \eta^{(1)}(x, t, \bar{x}, \bar{t}) = {} & \frac{A_m(\bar{x}, \bar{t})}{2}\exp(\mathrm{i}(k_m x - \omega t)) + \frac{A_n(\bar{x}, \bar{t})}{2}\exp(\mathrm{i}(k_n x - \omega t)) \\ & + \frac{-U^2 k_b b}{g\sinh(k_b h) - U^2 k_b \cosh(k_b h)}\frac{1}{2}\exp(\mathrm{i}k_b x) + \text{c.c.}, \end{aligned} \tag{A9}$$

in which the amplitudes of two unsteady wave components $A_m(\bar{x}, \bar{t})$ and $A_n(\bar{x}, \bar{t})$ are dependent on slowly-varying spatial and temporal coordinates. To find the evolution equations for $A_m(\bar{x}, \bar{t})$ and $A_n(\bar{x}, \bar{t})$, we need to consider the BVP at the next order.

A.2. *Second-order problem*

From (A3) to (A6), we have the second-order BVP for $\phi^{(2)}$,

$$\left.\begin{aligned} \phi_{xx}^{(2)} + \phi_{zz}^{(2)} &= D^{(2)}, \quad -h \leqslant z \leqslant 0, \\ \phi_{tt}^{(2)} + 2U\phi_{xt}^{(2)} + U^2\phi_{xx}^{(2)} + g\phi_z^{(2)} &= F^{(2)}, \quad z = 0, \\ \phi_z^{(2)} &= B^{(2)}, \quad z = -h, \end{aligned}\right\} \tag{A10}$$

in which the inhomogeneous forcing functions are given by

$$D^{(2)} = -2\phi_{\bar{x}x}^{(1)}, \tag{A11}$$

$$\begin{aligned} F^{(2)} = {} & -2[\phi_{\bar{t}t}^{(1)} + U\phi_{\bar{x}t}^{(1)} + U\phi_{x\bar{t}}^{(1)} + U^2\phi_{\bar{x}x}^{(1)}] \\ & - 2\{\phi_z^{(1)}[\phi_t^{(1)} + U\phi_x^{(1)}]_z + \phi_x^{(1)}[\phi_t^{(1)} + U\phi_x^{(1)}]_x\} \\ & - \eta^{(1)}[\phi_{ttz}^{(1)} + 2U\phi_{xtz}^{(1)} + U^2\phi_{xxz}^{(1)} + g\phi_{zz}^{(1)}] \end{aligned} \tag{A12}$$

and

$$B^{(2)} = \frac{\partial}{\partial x}[\phi_x^{(1)}\zeta(x)]. \tag{A13}$$

After substituting $\phi^{(1)}$ and $\eta^{(1)}$ into the forcing functions and dropping the non-secular terms, we have

$$\begin{aligned} D^{(2)} = &-\frac{gk_m}{\omega - k_m U}\frac{\cosh(k_m(z+h))}{\cosh(k_m h)}A_{m\bar{x}}(\bar{x},\bar{t})\exp(\mathrm{i}(k_m - \omega t)) \\ &-\frac{gk_n}{\omega - k_n U}\frac{\cosh(k_n(z+h))}{\cosh(k_n h)}A_{n\bar{x}}(\bar{x},\bar{t})\exp(\mathrm{i}(k_n - \omega t)) + \text{c.c.}, \end{aligned} \tag{A14}$$

$$\begin{aligned} F^{(2)} = &\, g(A_{m\bar{t}} + UA_{m\bar{x}})\exp(\mathrm{i}(k_m x - \omega t)) + \frac{1}{2}\frac{A_n U b k_b}{\mathbb{D}}\mathbb{M}[-\mathrm{i}\exp(\mathrm{i}(k_m x - \omega t))] \\ &+ g(A_{n\bar{t}} + UA_{n\bar{x}})\exp(\mathrm{i}(k_n x - \omega t)) + \frac{1}{2}\frac{A_m U b k_b}{\mathbb{D}}\mathbb{N}[-\mathrm{i}\exp(\mathrm{i}(k_n x - \omega t))] + \text{c.c.} \end{aligned} \tag{A15}$$

and

$$\begin{aligned} B^{(2)} = &-\frac{gA_m k_m k_n b}{4(\omega - k_m U)\cosh(k_m h)}[-\mathrm{i}\exp(\mathrm{i}(k_n x - \omega t))] \\ &-\frac{gA_n k_m k_n b}{4(\omega - k_n U)\cosh(k_n h)}[-\mathrm{i}\exp(\mathrm{i}(k_m x - \omega t))] + \text{c.c.}, \end{aligned} \tag{A16}$$

in which the coefficients $\mathbb{M}$, $\mathbb{N}$ and $\mathbb{D}$ take the form:

$$\begin{aligned} \mathbb{M} = &\, gk_n\frac{\omega - (k_n + k_b)U}{\omega - k_n U}(U^2 k_b\tanh(k_n h) - g) \\ &+ \frac{1}{2}\left[\frac{Ug^2k_n^2}{\omega - k_n U}\frac{1}{\cosh^2(k_n h)} + k_b(U^4k_b^2 - g^2)\right], \end{aligned} \tag{A17}$$

$$\begin{aligned} \mathbb{N} = &-gk_m\frac{\omega - (k_m - k_b)U}{\omega - k_m U}(U^2 k_b\tanh(k_m h) + g) \\ &+ \frac{1}{2}\left[\frac{Ug^2k_m^2}{\omega - k_m U}\frac{1}{\cosh^2(k_m h)} - k_b(U^4k_b^2 - g^2)\right], \end{aligned} \tag{A18}$$

$$\mathbb{D} = g\sinh(k_b h) - U^2 k_b\cosh(k_b h). \tag{A19}$$

A.3. *Solvability condition for the second-order BVP*

From the solvability condition for the second-order BVP, we can obtain the evolution equations for unsteady wave amplitudes A_m and A_n (Garabedian 1964; Mei *et al.* 2005). To do that, we express the solution of $\phi^{(2)}$ in the form

$$\phi^{(2)} = \Gamma_m(z,\bar{x},\bar{t})\exp(\mathrm{i}(k_m x - \omega t)) + \Gamma_n(z,\bar{x},\bar{t})\exp(\mathrm{i}(k_n x - \omega t)) + \text{c.c.} \tag{A20}$$

Upon substituting $\phi^{(2)}$ in (A20) into the BVP (A10) and using (A14), (A15), and (A16), we obtain the BVPs for unknown functions Γ_m and Γ_n, which are, respectively, expressed

in the following forms:

$$\left.\begin{aligned} \Gamma_{mzz} - k_m^2 \Gamma_m &= -\frac{gk_m}{\omega - k_m U} \frac{\cosh(k_m(z+h))}{\cosh(k_m h)} A_{m\bar{x}}, \quad -h \leqslant z \leqslant 0, \\ -\frac{(\omega - k_m U)^2}{g} \Gamma_m + \Gamma_{mz} &= A_{m\bar{t}} + U A_{m\bar{x}} - \mathrm{i} \frac{A_n U b k_b}{2\mathbb{D} g} \mathbb{M}, \quad z = 0, \\ \Gamma_{mz} &= \mathrm{i} \frac{g b k_m k_n}{4(\omega - k_n U)\cosh(k_n h)} A_n, \quad z = -h, \end{aligned}\right\} \tag{A21}$$

and

$$\left.\begin{aligned} \Gamma_{nzz} - k_n^2 \Gamma_n &= -\frac{gk_n}{\omega - k_n U} \frac{\cosh(k_n(z+h))}{\cosh(k_n h)} A_{n\bar{x}}, \quad -h \leqslant z \leqslant 0, \\ -\frac{(\omega - k_n U)^2}{g} \Gamma_n + \Gamma_{nz} &= A_{n\bar{t}} + U A_{n\bar{x}} - \mathrm{i} \frac{A_m U b k_b}{2\mathbb{D} g} \mathbb{N}, \quad z = 0, \\ \Gamma_{nz} &= \mathrm{i} \frac{g b k_m k_n}{4(\omega - k_m U)\cosh(k_m h)} A_m, \quad z = -h. \end{aligned}\right\} \tag{A22}$$

The corresponding homogeneous problem for Γ_m (and Γ_n) can be described in terms of a function $\psi(z)$ as

$$\left.\begin{aligned} \psi_{zz} - k_m^2 \psi &= 0, \quad -h \leqslant z \leqslant 0, \\ -\frac{(\omega - k_m U)^2}{g} \psi + \psi_z &= 0, \quad z = 0, \\ \psi_z &= 0, \quad z = -h. \end{aligned}\right\} \tag{A23}$$

A simple solution of this homogeneous problem is

$$\psi(z) = \cosh(k_m(z+h)). \tag{A24}$$

By applying Green's second identity with Γ_m and ψ and using the relations in (A21) and (A23), we shall obtain the evolution equation for A_m. Similarly, the application of Green's second identity with Γ_n and ψ gives the evolution equation for A_n. The final form of the spatio-temporal evolution equations for A_m and A_n is expressed as

$$\left.\begin{aligned} \frac{\partial A_m}{\partial t} + C_m \frac{\partial A_m}{\partial x} &= \mathrm{i} A_n \mathbb{P}, \\ \frac{\partial A_n}{\partial t} + C_n \frac{\partial A_n}{\partial x} &= \mathrm{i} A_m \mathbb{Q}, \end{aligned}\right\} \tag{A25}$$

in which the coefficients are given by

$$C_m = \frac{\omega - k_m U}{k_m} \frac{1}{2} \left(1 + \frac{2k_m h}{\sinh(2k_m h)}\right) + U, \tag{A26}$$

$$C_n = \frac{\omega - k_n U}{k_n} \frac{1}{2} \left(1 + \frac{2k_n h}{\sinh(2k_n h)}\right) + U, \tag{A27}$$

$$\mathbb{P} = \left[\frac{g b k_m k_n}{4(\omega - k_n U)\cosh(k_m h)\cosh(k_n h)} + \frac{U b k_b}{2\mathbb{D} g} \mathbb{M}\right] \tag{A28}$$

and

$$\mathbb{Q} = \left[\frac{g b k_m k_n}{4(\omega - k_m U)\cosh(k_m h)\cosh(k_n h)} + \frac{U b k_b}{2\mathbb{D} g} \mathbb{N}\right]. \tag{A29}$$

References

Binnie, A.M. 1960 Self-induced waves in a conduit with corrugated walls. I. Experiments with water in an open horizontal channel with vertically corrugated sides. *Proc. R. Soc. Lond.* A **259**, 18–27.

Buckles, J., Hanratty, T.J. & Adrian, R.J. 1984 Turbulent flow over large-amplitude wavy surfaces. *J. Fluid Mech.* **140**, 27–44.

Fan, J., Zheng, J.-H., Tao, A.-F., Yu, H.-F. & Wang, Y. 2016 Experimental study on upstream-advancing waves induced by currents. *J. Coast. Res.* **75** (sp1), 846–850.

Garabedian, P.R. 1964 *Partial Differential Equations*. John Willey and Sons.

Hasselmann, K. 1967 A criterion for nonlinear wave stability. *J. Fluid Mech.* **30** (4), 737–739.

Hudson, J.D., Dykhno, L. & Hanratty, T.J. 1996 Turbulence production in flow over a wavy wall. *Exp. Fluids* **20** (4), 257–265.

Kennedy, J.F. 1963 The mechanics of dunes and antidunes in erodible-bed channels. *J. Fluid Mech.* **16** (4), 521–544.

Kirby, J.T. 1988 Current effects on resonant reflection of surface water waves by sand bars. *J. Fluid Mech.* **186**, 501–520.

Kuzan, J.D., Hanratty, T.J. & Adrian, R.J. 1989 Turbulent flows with incipient separation over solid waves. *Exp. Fluids* **7** (2), 88–98.

Kyotoh, H. & Fukushima, M. 1997 Upstream-advancing waves generated by a current over a sinusoidal bed. *Fluid Dyn. Res.* **21** (1), 1–28.

Lamb, H. 1932 *Hydrodynamics*. Cambridge University Press.

McHugh, J.P. 1986 The stability of stationary waves produced by flow through a channel with wavy sidewalls. PhD thesis, The University of Michigan.

McHugh, J.P. 1988 The stability of stationary waves in a wavy-walled channel. *J. Fluid Mech.* **189**, 491–508.

McHugh, J.P. 1992 The stability of capillary-gravity waves on flow over a wavy bottom. *Wave Motion* **16** (1), 23–31.

Mei, C.C. 1969 Steady free surface flow over wavy bed. *J. Engng Mech. Div.* **95** (6), 1393–1402.

Mei, C.C. 1985 Resonant reflection of surface water waves by periodic sandbars. *J. Fluid Mech.* **152**, 315–335.

Mei, C.C., Stiassnie, M. & Yue, D.K.-P. 2005 *Theory and Applications of Ocean Surface Waves*. World Scientific.

Phillips, O.M. 1966 *The Dynamics of the Upper Ocean*. Cambridge University Press.

Raj, R. & Guha, A. 2019 On Bragg resonances and wave triad interactions in two-layered shear flows. *J. Fluid Mech.* **867**, 482–515.

Richardson, A.R. 1920 VIII. Stationary waves in water. *Lond. Edinb. Dubl. Phil. Mag. J. Sci.* **40** (235), 97–110.

Schlichting, H. & Gersten, K. 2017 *Boundary-Layer Theory*. Springer.

Shen, L., Zhang, X., Yue, D.K.P. & Triantafyllou, M.S. 2003 Turbulent flow over a flexible wall undergoing a streamwise travelling wave motion. *J. Fluid Mech.* **484**, 197–221.

White, F.M. 2006 *Viscous Fluid Flow*. McGraw-Hill.

Yih, C.-S. 1976 Instability of surface and internal waves. In *Advances in Applied Mechanics*, vol. 16, pp. 369–419. Elsevier.

Zilker, D.P. & Hanratty, T.J. 1979 Influence of the amplitude of a solid wavy wall on a turbulent flow. Part 2. Separated flows. *J. Fluid Mech.* **90** (2), 257–271.